Biomaterials Science

ROYAL SOCIETY OF CHEMISTRY

REVIEW

View Article Online
View Journal | View Issue

Cite this: *Biomater. Sci.*, 2023, **11**, 5108

Development of organic photosensitizers for antimicrobial photodynamic therapy

Wenya Zhou, Xiqun Jiang and Xu Zhen *

Received 28th April 2023,
Accepted 15th June 2023

DOI: 10.1039/d3bm00730h

rsc.li/biomaterials-science

Bacterial infection poses a significant threat to human health, and the emergence of antibiotic-resistant strains has exacerbated the situation. Antimicrobial photodynamic therapy (aPDT) has emerged as a promising antibiotic-free treatment option that employs reactive oxygen species (ROS) to cause oxidative damage to bacteria and surrounding biomolecules for treating microbial infections. This review summarizes the recent progress in the development of organic photosensitizers, including porphyrins, chlorophyll, phenothiazines, xanthenes and aggregation-induced emission photosensitizers, for aPDT. A detailed description of innovative therapeutic strategies that rely on the infection microenvironment or the unique structural properties of bacteria to amplify the therapeutic effects is provided. Moreover, the combination of aPDT with other therapy strategies such as antimicrobial peptide therapy, photothermal therapy (PTT) or gas therapy, is described. Finally, the current challenges and perspectives of organic photosensitizers for clinical antibacterial applications are discussed.

Introduction

Bacterial infections are a major global health threat, with severe skin lesions and infections causing nearly one million deaths worldwide each year.[1,2] The discovery of penicillin opened the door to a new era of antibiotics and led to the development of numerous antibiotics. However, antibiotics have been used as a panacea and are sometimes overused, resulting in the emergence of antibiotic-resistant "superbugs" and the inevitable failure of traditional antibiotics.[3,4] Antibiotic resistance causes millions of illnesses worldwide each year, and according to a recent survey by the U.S. Centers for Disease Control and Prevention, the number of deaths due to antibiotic resistance could reach tens of millions by 2050.[5,6] Moreover, bacteria can colonize the surfaces of many tissues or organs to form biofilms, which provide a strong protective barrier against various diseases such as periodontitis, eye infections, urinary tract infections, and respiratory tract infections.[7] Biofilms can also attach to the surface of biological materials, and over 80% of microbial infectious diseases are

State Key Laboratory of Analytical Chemistry for Life Science and Department of Polymer Science & Engineering, College of Chemistry & Chemical Engineering, Nanjing University, Nanjing, 210093, P. R. China. E-mail: zhenxu@nju.edu.cn

Wenya Zhou

Wenya Zhou is currently pursuing her Ph.D. in the School of Chemistry and Chemical Engineering at Nanjing University, under the supervision of Prof. Xu Zhen. Her current research interest is in the development of novel organic photosensitizers for antimicrobial photodynamic therapy applications.

Xiqun Jiang

Prof. Xiqun Jiang has been working at the School of Chemistry and Chemical Engineering, Nanjing University since 1986. He received his Ph.D. in Polymer Materials and Engineering from Nanjing University in 1998. His research interests include macromolecular self-assembly, molecular imaging probes, polymer drug delivery systems, and precise modification and biomedical applications of peptide- or protein-based biomaterials.

caused by biofilms.[8,9] To address these issues, researchers have studied and categorized the antimicrobial mechanisms of antibiotics in detail and combined two or even multiple antibiotics to achieve better efficacy.[10,11] However, such a strategy inevitably causes cross-resistance or multi-resistance, leading to suboptimal therapeutic effects with certain side effects.[12,13] Thus, there is an urgent need for the development of alternative strategies to treat bacterial infections.

Photodynamic therapy (PDT) has gained significant attention, primarily for cancer treatment.[14–22] However, in the 1990s, researchers discovered the potential of PDT as a powerful tool for combating bacterial infections. Antimicrobial photodynamic therapy (aPDT) employs photosensitizers that produce highly toxic reactive oxygen species (ROS) upon irradiation with an appropriate excitation light source, causing oxidative damage to surrounding lipids, proteins and nucleic acids and ultimately killing pathogenic microorganisms.[23] This strategy offers numerous advantages, including non-invasiveness, broad antibacterial spectrum, less susceptibility to drug resistance, and local treatment.[24,25] Notably, phenothiazine photosensitizer-mediated aPDT has been tested clinically for diabetic lower extremity ulcer infections and oral infections.[26] The photosensitizer undergoes a transition from its ground state to a transient single excited state upon light activation, and then through intersystem crossing (ISC) to a prolonged triple excited state.[27] On the one hand, photosensitizers in the triplet excited state react directly with the surrounding substrates through electron transfer to produce free radicals or radical ions, such as $^{\bullet}OH$ and $O_2^{\bullet-}$ (type I mechanism, mainly occurs on the bacterial cell membrane), leading to the formation of lipid peroxides that impair the bacterial structural integrity and increase the ionic permeability of the cell membrane. On the other hand, photosensitizers in the triplet excited state can also transfer energy with O_2 to form $^1O_2$ (type II mechanism), which is the most threatening ROS that directly causes oxidative damage to biological molecules such as unsaturated lipids, DNA, enzymes and other cell components, resulting in the effective killing of bacteria.[28,29] Meanwhile, in the realm of aPDT, it is crucial to consider the variances in the cell wall structure exhibited by Gram-positive and Gram-negative bacteria. Gram-positive bacteria display a robust and porous cell envelope characterized by extensive networks of peptidoglycan, teichoic acid and lipoteichoic acids, allowing the efficient penetration of small molecular compounds through the cell wall. In contrast, Gram-negative bacteria possess a distinctive bilayer structure, wherein the outer membrane presents a dense layer comprising negatively charged lipopolysaccharides and lipoproteins. This outer membrane functions as a formidable permeable barrier, significantly impeding the penetration of photosensitizers into the bacterial cell wall. Consequently, the divergent membrane structures of Gram-positive and Gram-negative bacteria engender varying levels of effectiveness in aPDT interventions.[30]

Hematoporphyrin derivatives are first-generation photosensitizers, among which Photofrin is widely used in various cancers. However, its clinical application is restricted by its inherent defects including poor chemical purity, a long half-life, a low molar attenuation coefficient and an ultra-short activation wavelength.[31] To achieve efficient aPDT treatment, photosensitizers must possess attributes such as excellent light stability, significant generation of ROS under light irradiation, and non-toxicity to normal tissues.[32,33] Moreover, the unique microenvironment of bacterial infection sites including hypoxia, pH reduction and H_2O_2 overexpression and the structural properties of bacteria such as the unique outer membrane structures in Gram-negative bacteria demand further optimization of photosensitizer design.[34–36] While inorganic photosensitizers such as carbon nanomaterials (carbon dots, fullerenes, *etc.*), gold nanomaterials, titanium dioxide, copper sulfide and black phosphorus offer advantageous photophysical properties of high photostability, they exhibit inherent limitations, including challenges associated with metabolism and high cytotoxicity.[5,23] In contrast, organic photosensitizers such as porphyrins, methylene blue (MB) and BODIPY possess favorable biocompatibility. However, their short absorption wavelength and suboptimal photostability hinder their widespread application in deep tissue infection treatment.[31,37] Although recent reviews have discussed the progress of organic photosensitizers used for aPDT, these reviews mainly focus on the design of organic photosensitizers for aPDT, with minimal elaboration on the various design strategies based on the microenvironment of the infection site or the structural properties of bacteria.[28,38,39] In this review, we summarize the advances in the development of organic photosensitizers including porphyrins, chlorophyll, phenothiazines, xanthenes and aggregation-induced emission photosensitizers for aPDT (Fig. 1). The design strategies of various organic photosensitizers are discussed. The innovative therapeutic strategies that rely on the infection microenvironment or the unique structural properties of bacteria to amplify the therapeutic effects are introduced in detail. Furthermore, the combination of aPDT with other therapy strategies such as antimicrobial peptide therapy, photothermal therapy (PTT) or gas therapy is described. Finally, the challenges and future development directions for organic photosensitizers in clinical antimicrobial applications are given.

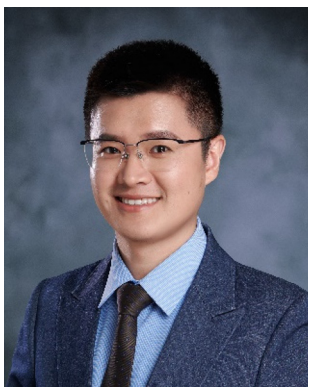

Xu Zhen

Prof. Xu Zhen received his Ph.D. in Chemistry from Nanjing University in 2014 followed by postdoctoral studies at the National University of Singapore (2014–2015) and Nanyang Technological University (2015–2018). He joined Nanjing University as an Associate Professor in 2019. His research interests focus on the development of smart molecular probes and nanomedicines for precision diagnosis and therapy.

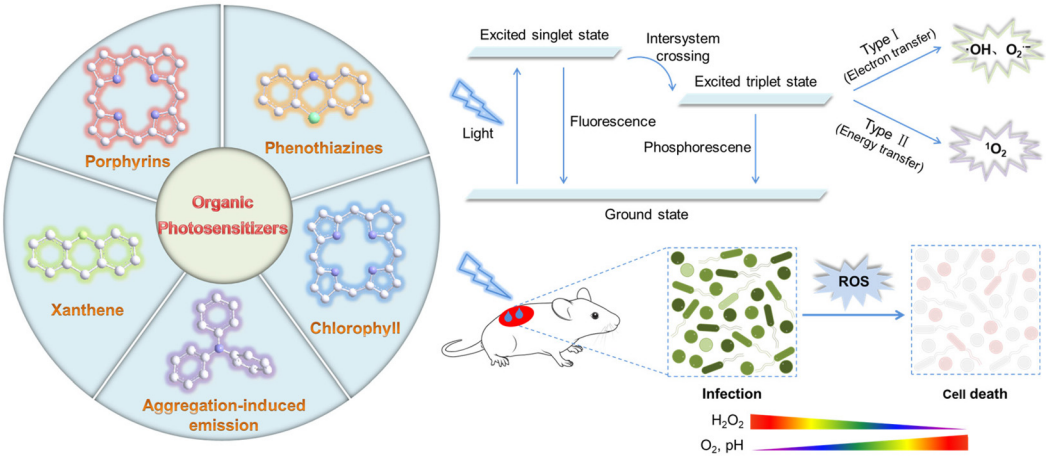

Fig. 1 Schematic representation of different organic photosensitizers in aPDT and the ROS generation mechanism.

Porphyrin photosensitizers

Porphyrin and its derivatives, which comprise tetrapyrrole subunits linked by methane bridges, are second-generation photosensitizers.[31] Due to their peak light absorption in the visible region, fast triplet state formation, high quantum yield and adaptable structural characteristics, they are considered ideal candidates for aPDT. As the first photosensitizer approved by the U.S. Food and Drug Administration, porphyrins have been extensively employed in various fields, showing potential for both anticancer and antibacterial activities.

To treat *S. mutans* biofilm-induced dental diseases and to whiten teeth, Zhang's group developed a bifunctional porphyrin (ZMP) composed of protoporphyrin (PP) and a hydrophilic zwitterion moiety (Fig. 2a).[40] The unique electron donor–acceptor structure and water solubility of ZMP significantly increased the ROS generation capacity, which was approximately 8-fold higher than that of PP under purple light irradiation, and displayed a powerful antibacterial effect toward *S. aureus* and *S. mutans*. Subsequently, teeth isolated from humans were further used to verify the feasibility of photodynamic biofilm eradication, and approximately 95% of *S. mutans* in tooth biofilms were killed by 125 μM ZMP upon irradiation for 10 min (Fig. 2b). After rinsing three times with saline, which mimics daily gargling, approximately 95% of *S. mutans* encased in the biofilm was washed away. In addition, ROS produced by 100 μM ZMP upon irradiation for 30 min could degrade 75% IC (colorant), and the stained teeth were significantly whitened after 6 h with an increase in whiteness. Different from 30% H_2O_2, the crowns of the teeth with 0.1 mm ZMP photodynamic whitening still showed a regular honeycomb after 6 h, which was the same as in normal crowns and did not corrode the tooth enamel.

In addition, a growing number of researchers are combining PDT with other therapies to achieve optimal treatment outcomes.[41–44] To treat wound infections, Zhang's group proposed a synergistic therapy based on photodynamic therapy and iron-blocking antibacterial therapy (IBAT) and designed cationic heme-mimetic gallium porphyrin (Ga-CHP) (Fig. 2c).[45] Ga-CHP showed good solubility in aqueous solution and obvious UV absorption at 410 nm and showed excellent ROS production under blue light irradiation. Iron is an essential nutrient for the survival of almost all bacteria, Ga-CHP mimicked the structure of heme and could be easily ingested by bacteria, which had little depolarization effect on the bacterial cell membrane at lethal concentrations, and SEM showed that the morphology of bacteria was still intact. The activity of catalase in *S. aureus* was lost after Ga-CHP entered the cytoplasm, which was a heme-requiring enzyme with heme as its auxiliary base. The inactivation of catalase would lead to the deterioration of the oxidation defense ability of bacteria, and heme in FAD medium antagonized the antibacterial activity of Ga-CHP against *S. aureus*. A great deal of ROS was produced in *S. aureus* after co-culture with Ga-CHP (2 MBC). They then evaluated the antibacterial activities of Ga-CHP, which was limited against *S. aureus* and *E. coli* by IBAT alone without light irradiation. The antibacterial effect was greatly improved after blue light irradiation, and the combination of photodynamic therapy and IBAT showed a synergistic effect. Subsequently, a mouse model of full-layer skin infection with *S. aureus* was established, Ga-CHP was injected intravenously, and the wounds were monitored and histologically analyzed. Ga-CHP + L showed a better effect in accelerating wound healing, with no obvious inflammatory cells, the lowest content of the inflammatory factor IL-6, and more collagen and CD31 (Fig. 2d). Recently, Zhou's group constructed a novel Janus Au-porphyrin polymersome (J-AuPPS) heterostructure, and the near field enhancement (NFE) effect between Au nanoparticles and porphyrin polymersomes (PPSs) enhanced the NIR light absorption and electric/thermal field intensity at their interface, improving energy transfer and energetic charge-carrier generation.[46] Compared with the non-Janus core-particle Au-PPS nanostructure (CP-AuPPS), J-AuPPS showed a higher photothermal conversion efficiency and $^1O_2$

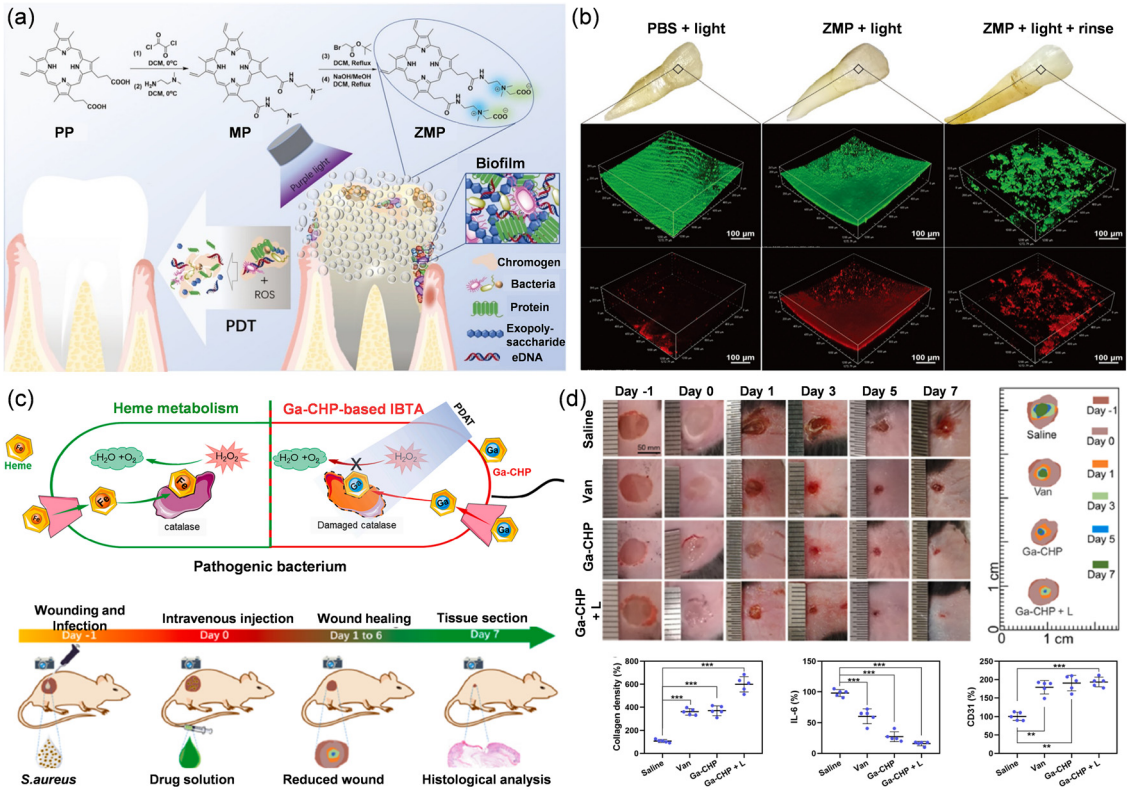

Fig. 2 (a) Synthetic route of ZMP and schematic illustration of using photodynamic dental therapy (PDDT) for tooth whitening and biofilm eradication. (b) Representative laser scanning confocal 3D images of the *S. mutans* biofilm on teeth after photodynamic antimicrobial treatment based on ZMP and PBS rinse.[40] Copyright 2021, Wiley-VCH. (c) Schematic diagram of the bacterial heme metabolism pathway and the proposed mechanism of Ga-CHP-based IBAT and PDAT. (d) Infected wound photographs of wounds at defined time points and quantitative analysis of collagen, IL-6 and CD31.[45] Copyright 2022, Elsevier.

yield under an 808 nm laser, which increased from 28.4% to 48.4% and 18% to 55%, respectively. For the treatment of chronic wounds, Sun *et al.* cooperated with photodynamic, photothermal and gaseous therapy to construct TP-Por CON@BNN6, which encapsulates the NO donor BNN6 into porphyrin-based COF nanosheets (Fig. 3a).[47] TP-Por CON@BNN6 showed high antibacterial activity against *E. coli* and *S. aureus*, while showing low phototoxicity and a low hemolysis rate against normal cells. It has also been shown to be effective in promoting the healing of *S. aureus*-infected chronic wounds and might degrade into small molecules under physiological conditions.

Significant changes in the microenvironment at the site of infection occur, including the overexpression of H_2O_2, hypoxia and pH reduction.[38,48–50] Excessive H_2O_2 not only causes damage to normal cells but also promotes the overexpression of certain inflammatory factors, which is not conducive to the treatment of the infected site. Therefore, it is necessary to regulate the H_2O_2 content of the infection site. Hu *et al.* designed a multiporphyrin-structured nanozyme Co^{II}TBPP (bpy) *via* supramolecular self-assembly, exhibiting excellent catalase-like properties, which can decompose highly expressed H_2O_2 into O_2 in the microenvironment, alleviate tissue hypoxia in the microenvironment and reduce the excess H_2O_2 content (Fig. 3b).[51] A large amount of ROS was generated under 660 nm illumination, which caused the bursting of the bacterial cell membrane and leakage of the contents. The antibacterial efficacy was up to 95% *in vitro*, and was shown to be well-treatable in a model of *E. coli* in wound rats. To cope with bacteria in different O_2 environments, Zhang's group designed TMPyP that could respond to specific bacteria (Fig. 3c).[52] In an aerobic environment with aerobic bacteria (*B. subtilis* and *P. aeruginosa*), TMPyP, as a typical photosensitizer, showed an inhibition efficiency of more than 99.9% after white light irradiation. In the absence of O_2, TMPyP could be reduced *in situ* to phlorin by some facultative anaerobic bacteria with strong reducing ability (*B. subtilis* and *P. aeruginosa*). Phlorin exhibited strong NIR absorption and significant photothermal conversion with excellent antibacterial activity. Xia *et al.* took advantage of the acidic microenvironment at the site of infection to fabricate a pH-responsive supramolecular photosensitizer platform based on carboxylatopillar[5]arene (CP5) and quaternary ammonium-functionalized tetrafluorophenyl porphyrin (TFPPQA) *via* host–guest interactions (Fig. 3d).[53] When the supramolecular photosensitizer reached the acidic infection sites, the cationic QA group was separated from the cavities of anionic CP5 due to the formation of the neutral carboxylic acid CP5. Then the exposed cationic QA group could

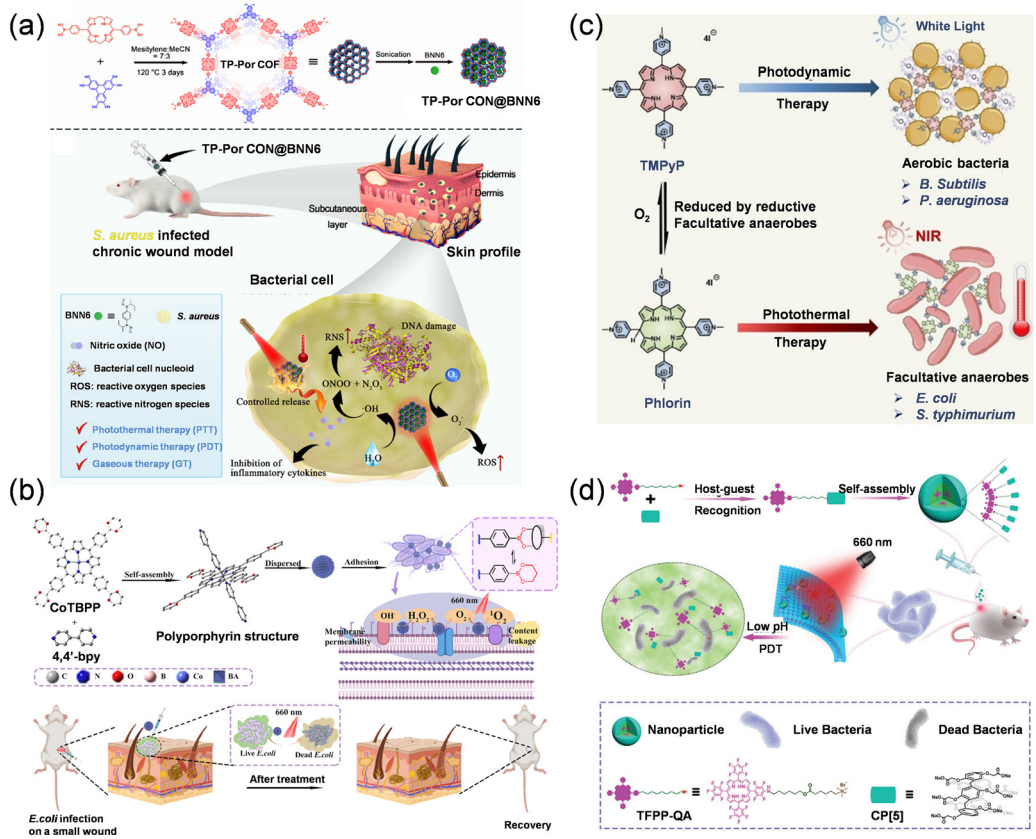

Fig. 3 (a) Schematic diagram of TP-Por CON@BNN6 destroying bacterial cells by synergistic therapy.[47] Copyright 2021, American Chemical Society. (b) Schematic presentation of the antibacterial mechanism of Co^{II}TBPP(bpy) in a skin ulcer infection model.[51] Copyright 2021, Elsevier. (c) Schematic illustration of bacteria-responsive TMPyP for adaptable PDT and PTT.[52] Copyright 2022, Wiley-VCH. (d) Schematic illustration of the antibacterial process of acid-triggered TFPP-QA/CP5.[53] Copyright 2021, Wiley-VCH.

target the negatively charged bacterial membrane, and further disrupt the charge balance of the bacterial membrane. Due to the penetrating ability of porphyrin photosensitizers and the therapeutic effect of PDT, TFPPQA/CP5 showed good antibacterial activity and biofilm dispersion ability. Aggregation-induced quenching (ACQ) photosensitizers such as porphyrin photosensitizers tend to accumulate and aggregate when applied to organisms due to their strong hydrophobicity, resulting in lower PDT efficiency. Yu *et al.* prepared an acid-triggered functional amphiphilic block copolymer POEGMA-*b*-[PDPA-*co*-PTPPC6MA] self-assembled of nanoparticles (PDPA-TPP) that rapidly dissociated bacterial microenvironments (pH 5.5).[54] This acid-triggered nanoplatform not only enhanced adhesion to bacterial cell membranes, but also solved the ACQ effect of porphyrin-based photosensitizers, resulting in a 5-fold increase in $^1O_2$ production.

Chlorophyll photosensitizers

Chlorophyll photosensitizers are a class of second-generation photosensitizers that differ from porphyrin photosensitizers in their structure. The chlorin photosensitizers replace a double bond with a single bond, which enhances their photosensitive effect in the red region.[37] Examples of chlorophyll photosensitizers include temoporfin, *p*-bro-mo-phenylhydrazone-methyl pyropheophorbide-a, chlorophyll-a, pheophorbide a, and chlorin e6 (Ce6).[55–57] Among these, Ce6 is a potent photosensitizer that has a wide range of applications in PDT, but its development has been hindered due to its poor water solubility and easy removal.[58]

To improve the efficiency of PDT in treating skin knife injury infection caused by Gram-negative bacteria, Fu's group constructed a novel polymer micelle (Pep@Ce6) with bacterial-targeting and photosensitizer loading capacity (Fig. 4a).[59] Pep@Ce6 was formed by supramolecular assembly of Ce6-conjugated α-cyclodextrin (α-CD-Ce6) and PEGylated polypeptide (PEG-Pep). The cationic Pep was able to penetrate the membrane of Gram-negative bacteria with its membrane destruction capability. Then, the micelle penetrated the weakened bacteria and Ce6 produced a large number of ROS in the presence of NIR irradiation, resulting in the death of the bacteria. The MIC value of Pep@Ce6 against *P. aeruginosa* with 660 nm irradiation was decreased to 64 μg mL^{-1} and demonstrated an excellent biofilm elimination effect. To effectively treat skin abscesses caused by *S. aureus* and prevent abscess recurrence,

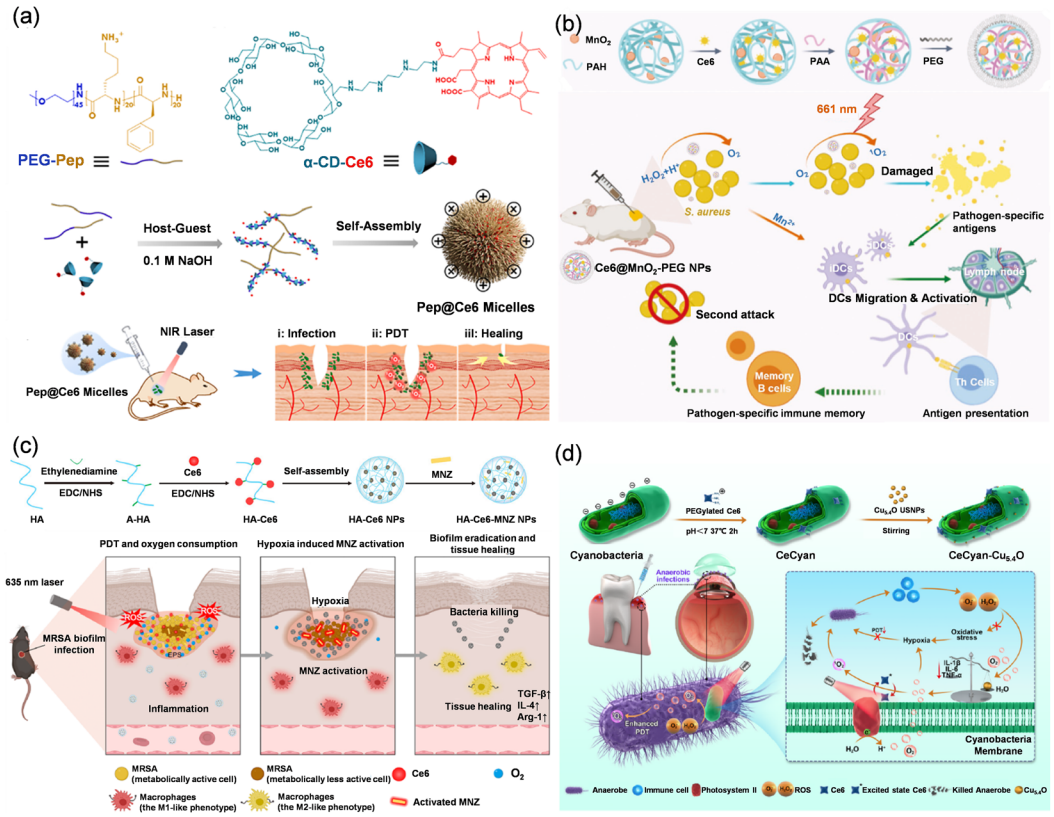

Fig. 4 (a) Schematic illustration of the cationic Pep@Ce6 micelles and antibacterial PDT for localized wound infections caused by *P. aeruginosa*.[59] Copyright 2021, Elsevier. (b) Schematic illustration of the synthesis of Ce6@MnO_2-PEG NPs and the related mechanisms of Ce6@MnO_2-PEG-based PDT for the treatment of *S. aureus* infections.[60] Copyright 202, WILEY-VCH. (c) Schematic illustration of the preparation of HCM NPs and the therapeutic processes of MRSA biofilms.[63] Copyright 2022, The Authors. (d) Schematic illustration of the fabrication of CeCyan-$Cu_{5.4}O$ and application in treating anaerobic bacterial infection.[64] Copyright 2022, The Authors.

Wang *et al.* developed Ce6@MnO_2-PEG NPs, which could modulate the microenvironment of abscesses, enhance the photodynamic treatment efficacy of skin abscesses and activate the immune system (Fig. 4b).[60] In Ce6@MnO_2-PEG NPs, MnO_2 nanoparticles were loaded with the photosensitizer Ce6 and modified with PEG, where MnO_2 could decompose excess H_2O_2 in the abscess microenvironment into O_2 and enhance the PDT efficiency. Ce6 and Ce6@MnO_2-PEG NPs showed similar great PDT efficacy against *S. aureus* in air, but were less effective in a nitrogen atmosphere. However, after the addition of H_2O_2 into the system, the antibacterial ability of Ce6@MnO_2-PEG NPs was significantly enhanced, while Ce6 still showed no improvements. Furthermore, during the PDT process, MnO_2 was degraded into Mn^{2+}, which acts as a natural immune stimulant of the STING pathway and can promote the immune response. Bacterial abscesses with Ce6@MnO_2-PEG NP-based PDT treatment showed a prominent increase in the proportion of mature DC ($CD11c^+CD80/CD86^+$) cells and IL-17 and IFN-γ levels, leading to significant immune responses. After 28 days of treatment, the percentage of memory B cells ($CD38^-/CD19^+$) in the peripheral blood of abscess-bearing mice increased significantly, the size of the abscess was the smallest and the recovery was the best after re-injection of *S. aureus*. Ce6@MnO_2-PEG NP-based PDT treatment could induce an effective immune memory response that prevents the recurrence of abscesses caused by the same type of bacterial infection. In order to improve the therapeutic efficacy against biofilms, Miao's group introduced a coating of water-soluble chitosan (WCS) onto iron oxide nanoparticles (IONPs). This modification endowed the nanoparticles with cationic properties, enabling the encapsulation of the anionic photosensitizer Ce6 and resulting in the formation of Ce6@WCS-IONPs with both cationic and small size characteristics.[61] Ce6@WCS-IONPs exhibited remarkable affinity for MRSA and demonstrated the ability to penetrate mature MRSA biofilms. This effective penetration led to a significant reduction in biofilm biomass and viable bacterial counts, highlighting the potent biofilm ablation activity of Ce6@WCS-IONPs.

Although PDT has promising antibacterial applications, its dependence on O_2 limits the therapeutic effect on the hypoxic microenvironment at the site of infection and even exacerbates hypoxia to a certain extent, further limiting the antibacterial effect.[14,62] There are two strategies to overcome this problem, one is to exploit the hypoxic microenvironment to design hypoxia-responsive drugs, and the other is to use oxygen-gen-

erating substances to improve the hypoxic microenvironment.[15] Considering that the bacteria with limited O_2 supply in the inner layer of the biofilm are typically in a state of low metabolic activity and exhibit high tolerance to antibiotics, resulting in incomplete bacterial killing and the recurrence of biofilm infection, Wang's group functionalized hyaluronic acid (HA) with the photosensitizer Ce6 and the prodrug metronidazole (MNZ) to form HA-Ce6-MnZ nanoparticles (HCM NPs) (Fig. 4c).[63] Once HCM NPs entered the infection site of the MRSA biofilm, they were decomposed by hyaluronidase (Hyal) secreted from MRSA to release Ce6 and MNZ. Ce6 could generate $^1O_2$ and kill bacteria in biofilms under normoxic conditions with 635 nm irradiation. The O_2 consumed by PDT subsequently exacerbates hypoxia in the biofilm and encourages the production of nitroreductase by MRSA, which further reductively activates MNZ by forming high toxicity imidazole fragments and kills MRSA with lower metabolic activity under hypoxic conditions. The anti-MRSA biofilm effect of HCM NPs was tested in diabetic mice, where infected wounds completely disappeared and the number of bacteria was decreased by 8 orders of magnitude after 12 days of treatment. In addition, infected tissues treated with HCM NPs exhibited less M1-like macrophage ($F4/80^+$ and $CD80^+$) infiltration and more M2-like macrophage ($F4/80^+$ and $CD206^+$) infiltration, accompanied by less secretion of TNF-α and IL-12p70 and more secretion of Arg-1 and IL-4, which greatly promoted the healing of infected wounds in mice. To alleviate the hypoxic microenvironment at the site of infection, Qu's group constructed CeCyan-$Cu_{5.4}O$ from the spontaneous oxygen-producing cyanobacteria supported photosensitizer Ce6 and ultrasmall $Cu_{5.4}O$ nanoparticles with catalase activity to eliminate anaerobic infections (Fig. 4d).[64] CeCyan-$Cu_{5.4}O$ completely eliminated *P. gingivalis*, *F. nucleatum* and *P. acnes* under anaerobic conditions with 660 nm irradiation (200 mW cm^{-2}, 2 min). Meanwhile, the O_2 produced by CeCyan-$Cu_{5.4}O$ destroyed the low oxygen saturation environment required for the growth of anaerobic bacteria and inhibited their growth. In animal models of anaerobic-infected keratitis and periodontitis, CeCyan-$Cu_{5.4}O$ not only presented good antibacterial activity, but also greatly reduced the inflammatory response, which is related to the nanozyme catalytic degradation ability of $Cu_{5.4}O$ toward ROS.

Gas therapy (including NO, CO, H_2S, *etc.*), as a new therapeutic mode, has aroused widespread attention because it does not produce drug resistance and plays a key role as an influential endogenous signaling molecule in a variety of biological processes.[65–68] Inspired by the favorable antimicrobial and biofilm-abating properties of gas therapy, numerous studies have combined gas therapy with PDT to achieve better efficacy. Cai's group reported a novel PDT-driven NO-controllable release system (Ce6@Arg-ADP), which was built using an L-Arg-rich amphiphilic dendritic peptide (Arg-ADP) as a carrier and loaded with Ce6 (Fig. 5a).[69] Ce6@Arg-ADP exhibited superior biofilm penetration performance, as demonstrated by the detection of a massive Ce6 fluorescence signal throughout the MRSA biofilms. After penetrating into the interior of the biofilm, Arg-ADP was oxidized to NO and L-citrulline by H_2O_2 produced during the PDT process. NO could react with $^1O_2$ to generate highly cytotoxic $ONOO^-$ and N_2O_3, further facilitating the rapid rupture of bacterial cell membranes and almost complete elimination of biofilms. Ce6@Arg-ADP combined PDT with NO to effectively treat subcutaneous abscesses, and NO promoted angiogenesis and promoted the migration and proliferation of various tissue repair cells to the wound tissue to accelerate wound healing. Similarly, Ji's group constructed a surface charge-switchable supramolecular nanocarrier, α-CD-Ce6-NO-DA, *via* the host–gust interaction of the GSH-sensitive NO/Ce6 prodrug (α-CD-NO and α-CD-Ce6) and pH-sensitive copolymer PEG-$(KLAKLAK)_2$-DA (Fig. 5b).[70] The surface charge of α-CD-Ce6-NO-DA was completely reversed from negative to positive when the pH was converted from physiological pH 7.4 to acidic pH 5.5, allowing it to efficiently penetrate the biofilm. On the one hand, once PDT-driven NO-controlled α-CD-Ce6-NO-DA penetrated into the biofilm, overexpressed GSH in the biofilm triggered the rapid release of NO, which not only produced large amounts of NO to kill bacteria, but also reduced the level of GSH in the biofilm to improve the efficiency of PDT. On the other hand, NO can react with ROS to generate RNS ($ONOO^-$), further improving the antibacterial efficiency. Ma *et al.* fabricated Ce6&CO@FADP using a fluorinated amphiphilic dendritic peptide (FADP) loaded with the Ce6 and CO prodrug (CORM-401) (Fig. 5c).[71] Fluorination of FADP favored the binding of Ce6&CO@FADP to bacteria and could provide O_2 for PDT. After entering the bacteria, Ce6&CO@FADP rapidly released CO in cells by consuming H_2O_2 produced during the PDT process. The combination of PDT and CO gas therapy provided significant synergistic biofilm eradication effects against subcutaneous bacterial infections and biofilm catheter models.

Phenothiazine photosensitizers

Phenothiazines, a class of cationic dyes, have recently garnered attention as effective antimicrobial photosensitizers due to their intensive absorption between 600 and 800 nm.[37] Among these, MB, a monocationic phenothiazine dye composed of a three-ring π-system with auxochromic side groups, is a well-established clinical treatment for chronic periodontitis and oral mucositis, and has demonstrated efficacy in light-induced plasma disinfection against drug-resistant strains and viruses. Similarly, other phenothiazine dyes, such as toluidine blue and Nile blue, have shown promise as organic photo-antimicrobials in the field of dentistry.[26]

Any modification in the surface of the phenothiazine skeleton has the potential to produce an improved PS, and most studies to date have focused on substitutions at the periphery of the tricyclic skeleton, discolored rings fused with other aromatic or alicyclic hydrocarbons, and sulfur substitutions in the central molecular scaffold.[72] On this basis, to selectively eradicate bacteria, Yoon's group designed two phenothiazinium photosensitizers, NBS-N and NBSe-N, with the same main structure but different elements (S/Se) (Fig. 6a).[73] Both

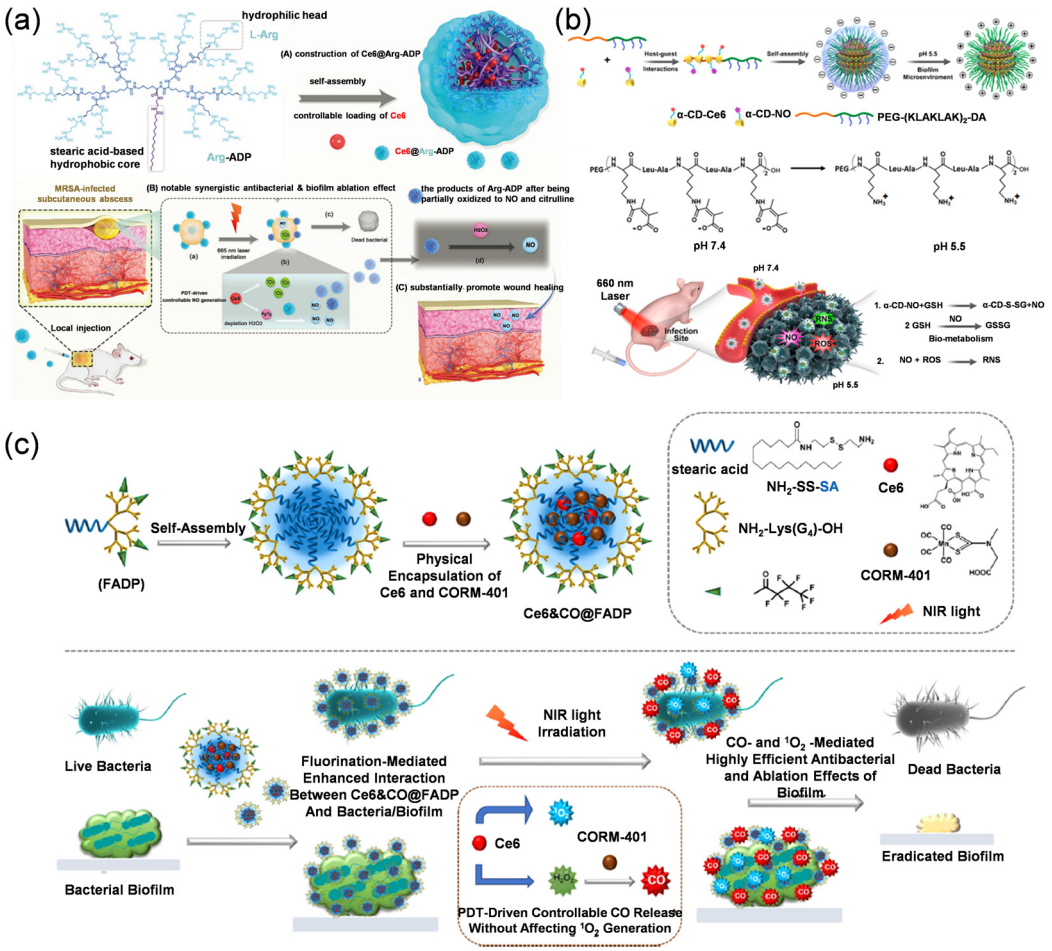

Fig. 5 (a) Schematic illustration of the preparation of Ce6@Arg-ADP and the related mechanisms for the highly efficient synergistic antibacterial and wound healing promotion effect of PDT/NO.[69] Copyright 2021, Wiley-VCH. (b) Schematic diagram of the preparation process of α-CD-Ce6-NO-DA nanocarriers and the related mechanisms of MRSA biofilm associated infection eradication by synergistic effects between ROS and NO.[70] Copyright 2020, American Chemical Society. (c) Schematic illustration of the preparation of Ce6&CO@FADP and the related mechanisms of PDT/CO synergistic antibacterial and ablation biofilms.[71] Copyright 2020, American Chemical Society.

NBS-N and NBSe-N could produce ROS under 655 nm laser irradiation (Fig. 6e), but NBS-N mainly produces $O_2^{\bullet-}$ and NBSe-N mainly produces $^1O_2$ (Fig. 6b–d), which may be caused by the substitution of the Se atom for the S atom and the increased triplet quantum yield. NBS-N and NBSe-N were able to penetrate into the membrane of *S. aureus* but barely penetrated the interior of *E. coli* due to the presence of the outer membrane. NBS-N with $O_2^{\bullet-}$ was able to selectively eradicate *S. aureus* over *E. coli*, while NBSe-N with $^1O_2$ exhibited promising killing efficacy against both *S. aureus* and *E. coli*. This may be because $O_2^{\bullet-}$ produced by NBS-N could be converted into highly reactive $^{\bullet}OH$ inside the bacteria rather than outside, and highly toxic $^1O_2$ can effectively destroy bacteria both inside and outside the outer membrane. Gao's group successfully synthesized phenothiazinium-based derivatives *via* a pyridine-fused strategy for the first time, which reduced *S. aureus* by 6 orders of magnitude under 30 J cm^{-2} light at 0.5 μM (0.21 ng mL^{-1}) and *E. coli* by 5 orders of magnitude under 50 J cm^{-2} light at 6 μM (2.52 ng mL^{-1}).[72]

To achieve deep tissue bactericidal capacity, and considering the severely short lifetime (*ca.* 3.5 μs) and diffusion limits (<0.3 μm) of $^1O_2$ in aqueous systems, the residual bacteria would continue to proliferate once the bacteria could not be completely removed by single PDT, Chen's group designed UCMB-LYZ-HP by fusing upconversion nanoparticles (UCNPs) with PDT and introducing lysozyme (LYZ) (Fig. 6f).[23,74] In this nanohybrid, b-$NaYF_4$:Yb,Er@$NaYF_4$ core–shell UCNPs were sequentially coated with dense silica and dendritic mesoporous silica for loading methylene blue (MB) and LYZ, respectively, and a bacterial hyaluronidase (HAase)-responsive valve was also introduced to realize controlled release of LYZ triggered by bacteria. UCMB showed maximum absorption at 590 and 654 nm, and strong $^1O_2$ production at 980 nm NIR irradiation within 12 min. UCMB-LYZ-HP was able to completely bind to MRSA within 240 s, effectively destroying the bacterial cell membrane and dramatically reducing MRSA by more than 5 orders of magnitude (Fig. 6g–j). To solve the problem that PDT is limited by bacterial communities embedded in the

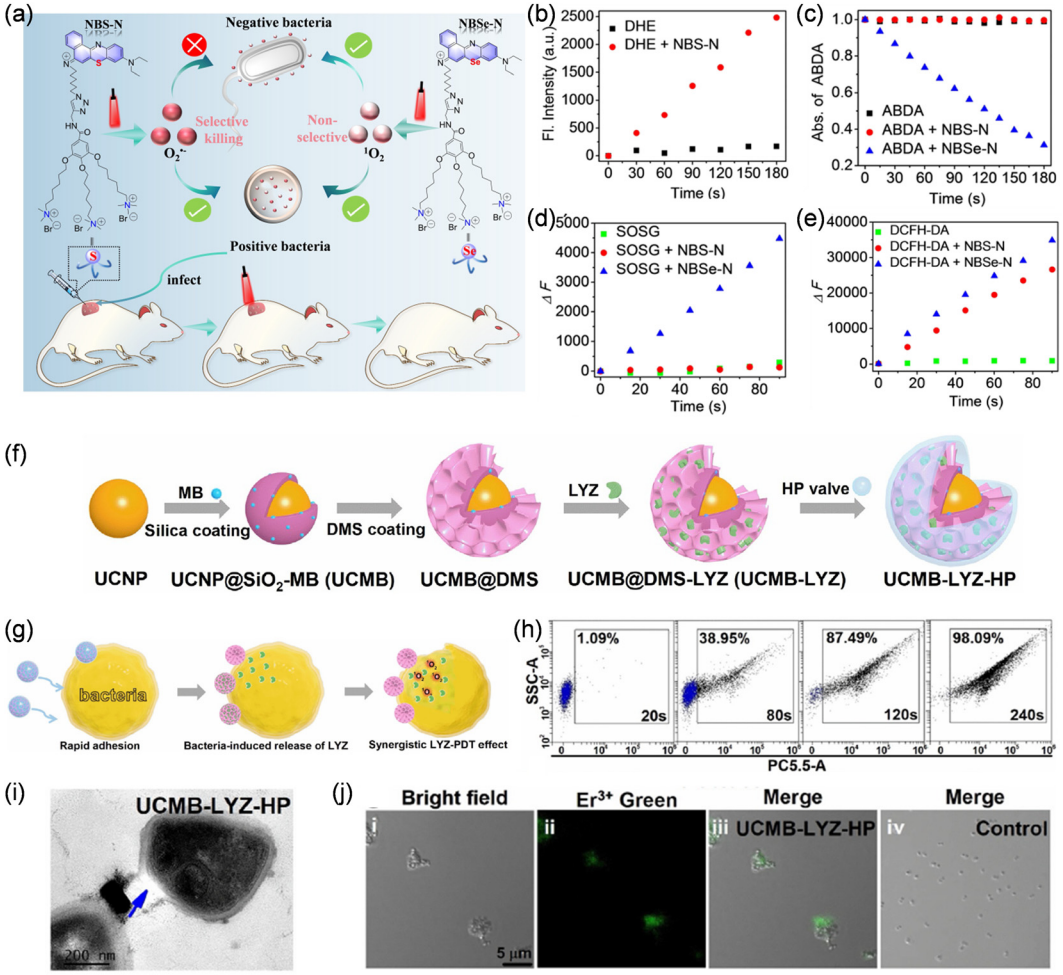

Fig. 6 (a) Schematic illustration of ROS generated by NBS-N and NBSe-N, and selective killing of Gram-positive bacteria and healing infected wounds of mice using NBS-N. (b) $O_2^{\cdot-}$ of NBS-N with ctDNA using DHE. $^1O_2$ generation in the presence of NBS-N and NBSe-N using (c) ABDA and (d) SOSG. (e) Total amount of ROS in NBS-N and NBSe-N using DCFH-DA.[73] Copyright 2022, Wiley-VCH. (f) Illustration of the fabrication of the antibacterial nanohybrid UCMB-LYZ-HP. (g) Proposed antibacterial mechanism of the nanohybrid based on synergistic enzymatic-photodynamic effects. (h) Binding kinetics of UCMB-LYZ-HP to MRSA. (i) Representative TEM images of MRSA after incubation with UCMB-LYZ-HP. (j) CLSM images of MRSA after incubation with UCMB-LYZ-HP.[74] Copyright 2021, Wiley-VCH.

dense extracellular matrix of mature biofilms, Balhaddad *et al.* designed MagTBO, a multifunctional photosensitizer nanoplatform, by combining toluidine blue *ortho* photosensitizer (TBO) with superparamagnetic iron oxide nanoparticles (SPIONs) *via* the microemulsion method.[75] In the presence of an external magnetic field, MagTBO was able to drive and penetrate deep inside the biofilm, extremely reducing the bacteria in the *S. mutans* biofilm by 6 orders of magnitude, demonstrating the feasibility of using a magnetic field as a navigation method to enhance the antibacterial effect of photosensitizers.

Xanthene photosensitizers

Xanthenes, a class of cyclic dyes comprising three linear aromatic rings and one oxygen atom, possess high quantum yield and excellent biocompatibility, rendering them ideal fluorescent probes for bioimaging. They also serve as photosensitizers, and the renowned halogenated derivative, Rose Bengal (RB), is widely used in the photodynamic treatment of tumors due to its potent photosensitizing effect.[58]

Bacteria in biofilms are insensitive to antibiotics (the effective dose required is 10–1000 times higher than that of planktonic bacteria), and extracellular polymeric substances (EPSs) in biofilms provide a mechanically stable environment for bacteria, preventing the penetration and subsequent action of antibiotics.[7,37,76] *P. aeruginosa*, the main cause of bacterial keratitis, shows natural resistance to antibiotics and forms stable biofilms. *P. aeruginosa* contains two lectins, Lec A (D-galactose-specific) and Lec B (L-focuse specific), which play critical roles in a series of pathological processes, making them attractive therapeutic targets. Zhu *et al.* constructed a series of block copolymers PαGal$_{50}$-*b*-PGRB$_n$ for the treatment

of multidrug-resistant biofilm-infected keratitis, in which PαGal$_{50}$ was used to improve the water solubility of PαGal$_{50}$-*b*-PGRB$_n$ to produce sufficient ROS for antibacterial activity, and α-D-galactose species were able to bind specifically to Lec A of *P. aeruginosa* (Fig. 7a).[77] Amphiphilic PαGal$_{50}$-*b*-PGRB$_n$ could self-assemble into micelles, in which the hydrodynamic diameter of PαGal$_{50}$-*b*-PGRB$_{20}$ was approximately 168 nm and produced a large amount of $^1O_2$ and $^{\bullet}OH$ under 578 ± 10 nm light irradiation. Similarly, ROS levels in MDR-*P. aeruginosa* also increased significantly after light treatment with PαGal$_{50}$-*b*-PGRB$_{20}$, which had a significant killing effect on MDR-*P. aeruginosa* (MIC value was 128 μg mL^{-1}) (Fig. 7b and c). However, the photodynamic killing effect of PαGal$_{50}$-*b*-PGRB$_{20}$ was sharply weakened by the addition of 0.1% trypsin to PαGal$_{50}$-*b*-PGRB$_{20}$, which destroyed the surface protein of MDR-*P. aeruginosa* and blocked the binding of α-D-galactose to Lec A. DNA and protein of MDR-*P. aeruginosa* were damaged after PαGal$_{50}$-*b*-PGRB$_{20}$ treatment (low relative residual ratio), and PαGal$_{50}$-*b*-PGRB$_{20}$ could reduce the expression level of virulence factors (las R, mvfR, rhlR and pvdA), which was beneficial for the elimination of the biofilm (Fig. 7d). PαGal$_{50}$-*b*-PGRB$_{20}$ could penetrate and disperse the MDR-*P. aeruginosa* biofilm, in which the bacteria in the biofilm were almost completely dead, and showed a better repair effect on rabbit keratitis infected with the MDR-*P. aeruginosa* biofilm (Fig. 7e–i).

In response to the increasing resistance of *P. aeruginosa* to antibiotics, Hu's group designed a dual-modality antimicrobial polymer PBMA-*b*-P(DMAEMA-*co*-EoS)-UBI, in which ubiquicidin (UBI$_{29–41}$, TGRAKRRMQYNRR) was an antimicrobial peptide with 6 positively charged residues, which has high affinity and specificity toward *P. aeruginosa* and exhibited significant membrane insertion, fusion, and damage capabilities (Fig. 8a).[78] In addition, *in situ* photodynamic activation of eosin Y (EoS) to produce $^1O_2$ under green light irradiation

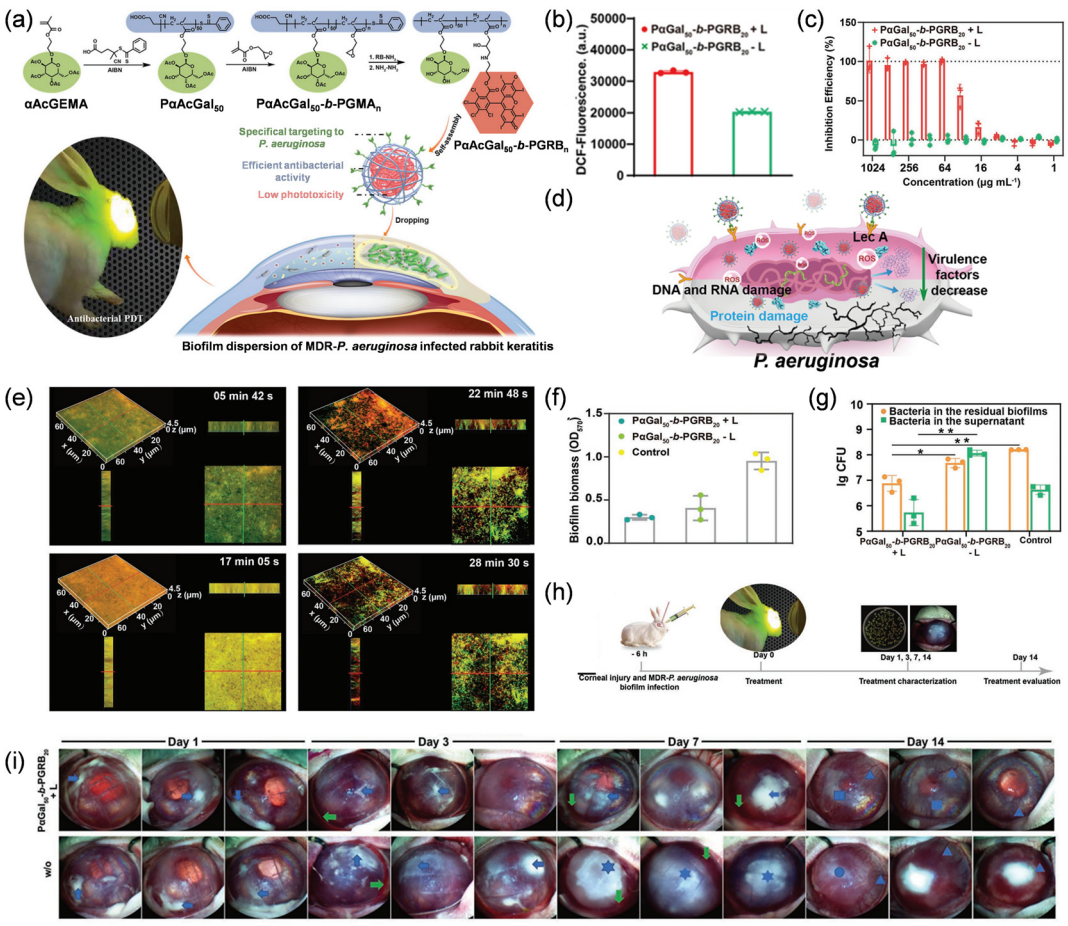

Fig. 7 (a) Schematic illustration of MDR bacterial-targeted nanoassembly and its bioapplication in an MDR-*P. aeruginosa* biofilm-infected rabbit keratitis model. (b) Intracellular ROS intensity produced by MDR-*P. aeruginosa* treated with PαGal$_{50}$-*b*-PGRB$_{20}$ under light irradiation. (c) Inhibition efficiency of PαGal$_{50}$-*b*-PGRB$_{20}$ against MDR-*P. aeruginosa* with or without light. (d) Schematic diagram of the antibacterial mechanism of PαGal$_{50}$-*b*-PGRB$_{20}$ against MDR-*P. aeruginosa*. (e) The penetration process through established MDR-*P. aeruginosa* biofilm dispersion and killing by PαGal$_{50}$-*b*-PGRB$_{20}$. (f) Quantitative statistical results of crystal violet-stained biofilms. (g) Statistical CFUs inside the established MDR-*P. aeruginosa* and in the supernatant with different treatments. (h) Illustration of the construction of the MDR-*P. aeruginosa* biofilm infected keratitis model and the therapeutic profile. (i) Representative corneal photographs of MDR-*P. aeruginosa* biofilm infected keratitis on rabbits of the treatment and untreated groups.[77] Copyright 2021, Wiley-VCH.

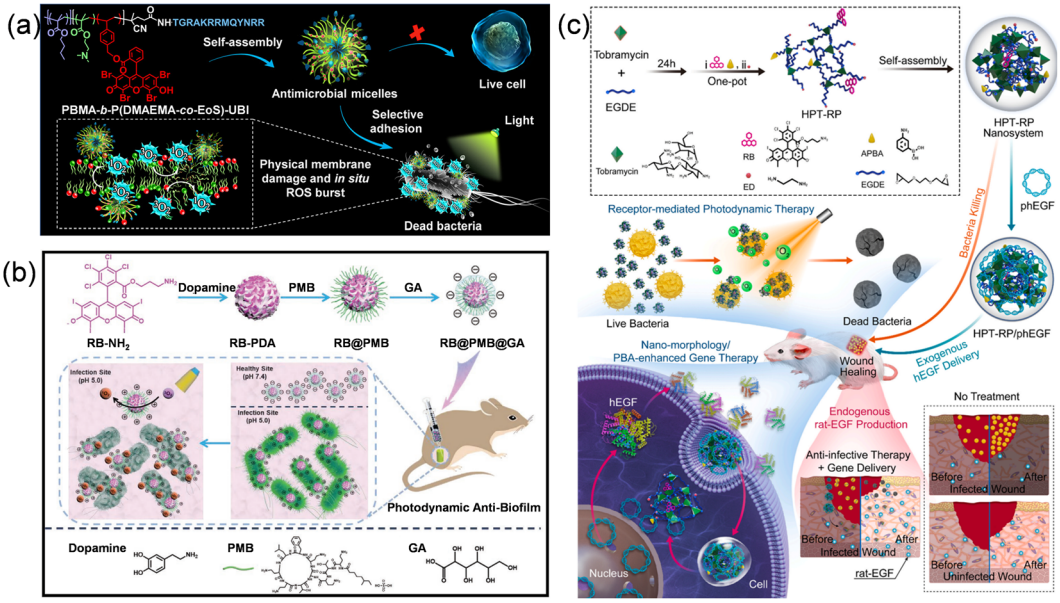

Fig. 8 (a) Schematic illustration of PBMA-*b*-P(DMAEMA-*co*-EoS)-UB significantly inhibiting Gram-negative bacteria *via* selective recognition of bacteria and fusion into the bacterial membrane.[78] Copyright 2019, American Chemical Society. (b) Schematic illustration of the preparation process of RB@PMB@GA NPs for enhanced penetration and antibacterial efficiency in biofilms.[79] Copyright 2021, Wiley-VCH. (c) Schematic illustration of the synthetic route of the HPT-RP nanosystem and its antibacterial/gene-delivery applications in infected wound healing.[80] Copyright 2021, Elsevier.

further destroyed the bacterial membrane, thereby eliminating the remaining persistent *P. aeruginosa*. Based on the synergistic effect of physical destruction and photodynamic therapy, PBMA-*b*-P(DMAEMA-*co*-EoS)-UBI showed excellent bacterial elimination and promoted wound healing in both knife injury and burn models of *P. aeruginosa*, which was equivalent to commercially available antibiotics. Furthermore, Wu *et al.* developed a pH-sensitive photodynamic nanosystem RB@PMB@GA NPs, in which the RB-PDA NP core was prepared by a covalent combination of the photosensitizer RB with polydopamine (PDA) and then prepared by layer-by-layer functionalization of polymyxin (PMB) and gluconic acid (GA) (Fig. 8b).[79] RB@PMB@GA NPs showed a slightly negative charge under physiological conditions (pH 7.4), which reduced cell internalization and had minimal toxicity to normal cells, but changed to a positive charge at the infection site (pH 5.0). The positively charged PMB was able to bind to the negatively charged outer membrane of Gram-negative bacteria, leading to the destabilization of the bacterial outer membrane and enhancing the photodynamic bactericidal effect against Gram-negative bacteria. The MIC/MBC value of RB@PMB@GA NPs against *P. aeruginosa* was greater than 256 μM at pH 7.4, but decreased to 4 μM under acidic conditions and achieved effective biofilm eradication *in vivo* in implanted catheter mouse models. To accelerate the healing of infected wounds, Shao *et al.* designed a bifunctional nanosystem HPT-RP for antibacterial and gene delivery, which was prepared by the ring-opening polymerization of tobramycin and diepoxy molecules and functionalized with phenylboronic acid (PBA) and RB (Fig. 8c).[80] HPT-RP could be self-assembled into nanoparticles, where PBA had superior affinity to various biomolecular/receptors and could be used to deliver therapeutic plasmid phEGF (encoding human EGF), exhibiting excellent antimicrobial capacity.

Aggregation-induced emission photosensitizers

Aggregation-induced emission luminogens (AIEgens) have garnered considerable attention as fluorescent probes due to their exceptional properties, including large Stokes shifts, high sensitivity, excellent photostability, and robust long-term tracking capability.[81,82] A notable aspect of AIEgens is their dual functionality, serving not only as diagnostic biological probes but also as therapeutic drugs in some cases.[83–88] AIEgens exhibit robust photosensitization ability and superior anti-photobleaching ability in the aggregated state. Consequently, AIEgens generally exhibit higher photodynamic efficiency than conventional photosensitizers.[89]

The photosensitizers can be excited into a singlet excited state and then into a triplet state *via* ISC by light illumination. Photosensitizers in the triplet state have a lengthy sufficient lifetime to react with the surrounding O_2 or substrate to produce ROS, including type II ROS through energy transfer (such as $^1O_2$) or type I ROS (such as $^{\bullet}OH$ or $O_2^{\bullet-}$) through electron transfer, which are less oxygen dependent than type II PDTS.[32,58,90–92] To generate more ROS, especially type I ROS, Liu *et al.* proposed a molecular cationization strategy by cationizing the pyridine of the neutral precursors TBZPy and CTBZPy to obtain two cationic AIE photosensitizers TBZPyI and CTBZPyI (Fig. 9a).[93] Unlike traditional D–A molecules, D–

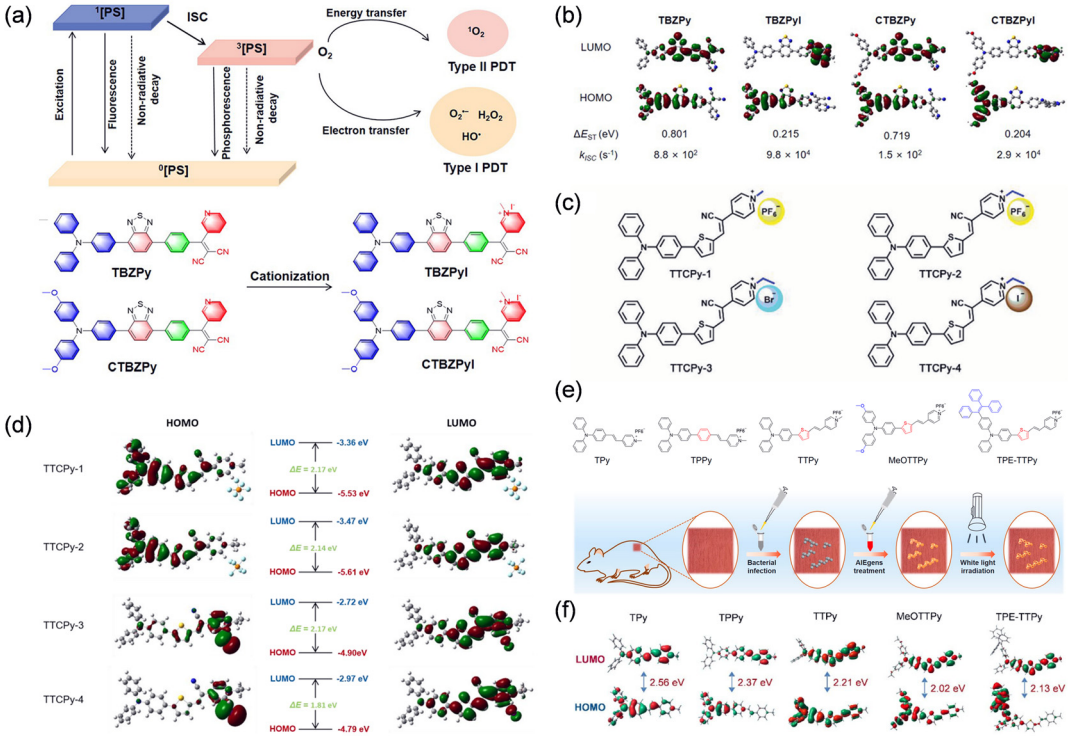

Fig. 9 (a) Schematics of the ROS generation mechanism and the molecular cationization approach to boost ROS generation. (b) HOMO and LUMO distribution, ΔE_{ST}, and k_{ISC} values of TBZPy, CTBZPy, TBZPyI and CTBZPyI.[93] Copyright 2022, American Chemical Society. (c) Molecular structures and (d) frontier molecular orbitals of TTCPy-1, TTCPy-2, TTCPy-3 and TTCPy-4.[94] Copyright 2021, The Authors. (e) Molecular structures and (f) frontier molecular orbitals of Tpy, TPPy, TTPy, MeOTTPy, and TPE-TTPy.[95] Copyright 2019, American Chemical Society.

A'–π–A AIEgens TBZPy and CTBZPy have triphenylamine (TPA) or methoxy-substituted triphenylamine (CTPA) as electron donors, benzothiadiazole and benzene as the co-acceptor and π-bridge, and cyano as the acceptor. These four photosensitizers showed obvious UV absorption at 450 to 520 nm. Compared with TBZPy and CTBZPy, the ROS generation capacity of cationized TBZPyI and CTBZPyI increased by 791.6 and 821.6 times, respectively, and the formation of $^{\bullet}OH$ increased from 17.7 and 17.9 to 47.5 and 172.9 after 20 seconds of exposure to a 520 nm laser, respectively. The reason for this is first because cationization leads to the formation of a methylpyridine group with stronger electron receptivity, leading to better HOMO–LUMO separation and lower ΔE_{ST} values (0.215 and 0.204), thus promoting a more efficient ISC process, which is essential for improved ROS production (Fig. 9b). Second, the introduction of cationic receptors also increased the intramolecular charge (ICT) effect, enhanced the electron separation and transfer ability, and greatly promoted the generation of type I ROS. In addition, the introduction of methoxy groups into triphenylamine can also increase the electron donating capacity of the donor and improve ROS production (CTBZPy > TBZPy, CTBZPyI > TBZPyI). In addition, CTBZPyI could be well bonded to the MRSA surface through electronic interactions due to the cationization of neutral CTBZPy. Similar to the above design concept, Xiao *et al.* designed four kinds of anion-π^{+} AIEgens (TTCPy-1, TTCPy-2, TTCPy-3, and TTCPy-4), chose triphenylamine as the electron donor, thiophene as the donor and π bridge, the carbon–carbon double bond as the π bridge, the cyano and pyridinium as electron receptors, changed the substituents on the pyridine salt and chose different anions as counterions to accurately adjust the D–A strength and ISC process (Fig. 9c).[94] The maximum UV absorption peaks of TTCPy-1, TTCPy-2, TTCPy-3 and TTCPy-4 in DMSO were 532, 532, 534 and 534 nm, respectively, and significant ROS were generated after 2 min of white light irradiation (superior to RB and Ce6). The ROS generation capacity of TTCPy-3 and TTCPy-4 was more remarkable (increased by approximately 550 times), which was due to the strong heavy atomic effect of bromine and iodide ions that promoted the ISC process. TTCPy-1, TTCPy-2, TTCPy-3 and TTCPy-4 exhibited strong $^{\bullet}OH$ and $O_2^{\bullet-}$ generation but weak $^1O_2$ generation after exposure to white light. The electron clouds of the HOMOs of these AIE-PSs were mostly delocalized in the triphenylamine part due to the orbital contribution of cyano and pyridinium groups, showing the separation of HOMOs and their typical D–A characteristics with HOMO–LUMO gaps of 2.17, 2.14, 2.17 and 1.81 eV, respectively (Fig. 9d). The ΔE_{ST} value (0.74 eV) of TTCPy-4 with iodide (I) as the counterion was the smallest among these AIE-PSs (1.22 eV, 1.20 eV and 1.15 eV, respectively), which can generate free radicals more efficiently. The oxidation potentials of TTCPy-1, TTCPy-2, TTCPy-3 and TTCPy-4 were 0.767, 0.709, 0.633 and 0.234 eV, respectively,

indicating that I and Br ions exhibited stronger electron-donating properties. These make it easier for excited TTCPy-3 and TTCPy-4 to acquire electrons from an electron-rich environment and transfer them to molecular oxygen *via* a type I mechanism than TTCPy-1 and TTCPy-2. To explore the structure–function relationship, Kang *et al.* designed TPy, TPPy, TTPy, MeOTTPy and TPE-TTP (Fig. 9e).[95] Their HOMO–LUMO energy gaps decreased gradually from 2.56 eV to 2.02 eV, with the maximum absorption peak in DMSO redshifted in the range of 427 to 500 nm, and the ROS generation efficiency was gradually enhanced under white light irradiation, all of which were due to the increasing order in the D–A interactions from TPy to MeOTTPy (Fig. 9f). In addition, Shi *et al.* proposed that limiting the rotation of some bonds could further inhibit nonradiative decay and thus promote the production of ROS.[96] Therefore, a series of carbazole group-based AIE photosensitizers (CPVBA, CPVBP, CPVBP2, and CPVBP3) with the rotation of two phenyl–N bonds being completely constrained and diphenyl amine group-based AIE photosensitizers (TPVBA, TPVBP, TPVBP2, and TPVBP3) were constructed. Due to the weaker electron-donating capacity of the carbazole, ΔE_{ST} of TTVBAs is smaller than that of CPVBAs, but the ROS generation of CPVBAs is stronger than that of TTVBAs. Restricting the rotation of the two phenyl–N bonds can increase the ROS generation of CPVBAs, even though ΔE_{ST} is larger, possibly because nonradiative decay is further inhibited, and the resulting extra energy is consumed by fluorescence and ISC processes. CPVBP3 with two positive charges was more readily taken up by Gram-negative bacteria and entered the bacteria to exert a photodynamic antibacterial effect. Zhou *et al.* synthesized an AIE-active benzothiadiazole and tetraphenylthene (TPE)-containing conjugated polymer (PTB-APFB).[97] Compared with the low-mass model compound MTB-APFB, the ΔE_{ST} value of PTB-APFB decreased from 1.773 to 0.881, with a 13-fold increase in ROS generation efficiency, exhibiting a superior healing rate compared to cefalotin in the treatment of *S. aureus*.

Peptidoglycan is an important component of the bacterial cell membrane, which is a short peptide network (L-Ala-D-Glu-*m*-Dap-D-Ala-D-Ala) of cross-linked repeated units of *N*-acetylglucosamine (GlcNAc) and *N*-acetylmuramic acid (MurNAc).[98] When bacteria are incubated with metabolic precursors such as D-amino acids and MurNAc modified with biological orthogonal functional groups, reactive chemical groups such as azides and alkynyl groups are expressed on the bacterial cell wall. The subsequent introduction of the corresponding biorthogonal group-modified compounds can be used to effectively tag bacterial peptidoglycans specifically *via* ligation reactions.[99] With the strength of metabolic biomolecular labeling technology, Liu's group designed d-AzAla@MIL-100 (Fe) nanoparticles (NPs) that preferentially accumulated at the site of infection *via* EPR effects (Fig. 10a).[100] MIL-100 (Fe), composed of iron(III) metal centers and trimesic acid (TMA) ligands, could catalyze the decomposition of H_2O_2 at the inflammation site, destroy the coordination between TMA and iron(III), and release the encapsulated d-AzAla, which was specifically ingested by bacteria and expressed on the bacterial wall. Ultrasmall 2-(1-(5-(4-(1,2,2-tris (4-methoxyphenyl)vinyl)phenyl)thiophen2-yl)ethylidene) malononitrile NPs (US-TPETM NPs) with AIE characteristics were then used as the labeling reagent. The DBCO groups were exposed to the surface of NPs and bound with bacteria *via* a click reaction, with the hydrophobic TPETM molecules encapsulated inside, which not only specifically tracked MRSA in infected skin tissue, but also precisely eradicated bacteria and reduced acute inflammation under light irradiation. To solve the problem that the current bioorthogonal reaction usually requires two-step operation, and may even require complex catalysts for the ligation reaction, they developed a metabolic probe TPEPy-D-Ala, which combined the AIE photosensitizer pyridinium-substituted tetraphenylethylene (TPEPy) with D-Ala (Fig. 10b).[101] TPEPy was small enough to allow TPEPy-D-Ala to participate in the metabolism of peptidoglycan in intracellular bacteria. Moreover, once TPEPy-D-Ala was ingested by bacterial peptidoglycan, the intramolecular motions were more or less restricted compared to its molecular state, and enhanced fluorescence enabled the monitoring of bacteria in living macrophages. The MIC of TPEPy-D-Ala toward intracellular MRSA was 20 ± 0.5 μg mL^{-1}, and MRSA cells in Raw 264.7 lost morphological integrity and presented fragmentation under white light irradiation, but showed low phototoxicity to Raw 264.7 cells. In a similar vein, they also designed a bacterial metabolism probe, TPACN-D-Ala, that specifically tracks bacteria on infected tissue in a single step of manipulation and ablation of bacteria sheltered in biofilms.[102] To diagnose early sepsis and disinfect extracorporeal blood efficiently, Gu's group proposed a novel synergistic strategy by combining AIEgens TBTCP-PMB with phages through a straightforward nucleophilic substitution reaction.[84] The resulting TBTCP-PMB engineered phages exhibited a unique combination of phages and photosensitizers, which could selectively identify bacterial species in human septic blood samples within 30 minutes, allowing visualization of the bacterial infection process and the subsequent discriminative eradication.

Based on previous reports of cationic AIEgens as a treatment for keratitis, Li *et al.* designed a cationic AIEgen TTPy with suitable hydrophobicity.[103] Driven by electrostatic and hydrophobic interactions, TTPy was able to rapidly identify and bind to *S. aureus*, and a large amount of ROS could be produced at a low concentration, effectively killing *S. aureus* without apparent cytotoxicity under white light irradiation. Most importantly, the high killing effect of TTPy induced an early innate immune response, rapid recruitment of neutrophils, and subsequent reduction of inflammatory bursts. This not only inhibited the spread of infection but also protected the retina from inflammation-related bystander tissue damage, effectively avoiding vision loss and providing a novel strategy for BE treatment. Furthermore, for the treatment of refractory keratitis, Wang's group constructed a NIR light-responsive nanofabricated platform core–shell structure UCNANs by combining on-demand NO therapy with PDT (Fig. 10c).[104] The nanoplatform used UCNPs ($NaYF_4$:Yb^{3+},Tm^{3+}@$NaYF_4$:Nd^{3+},

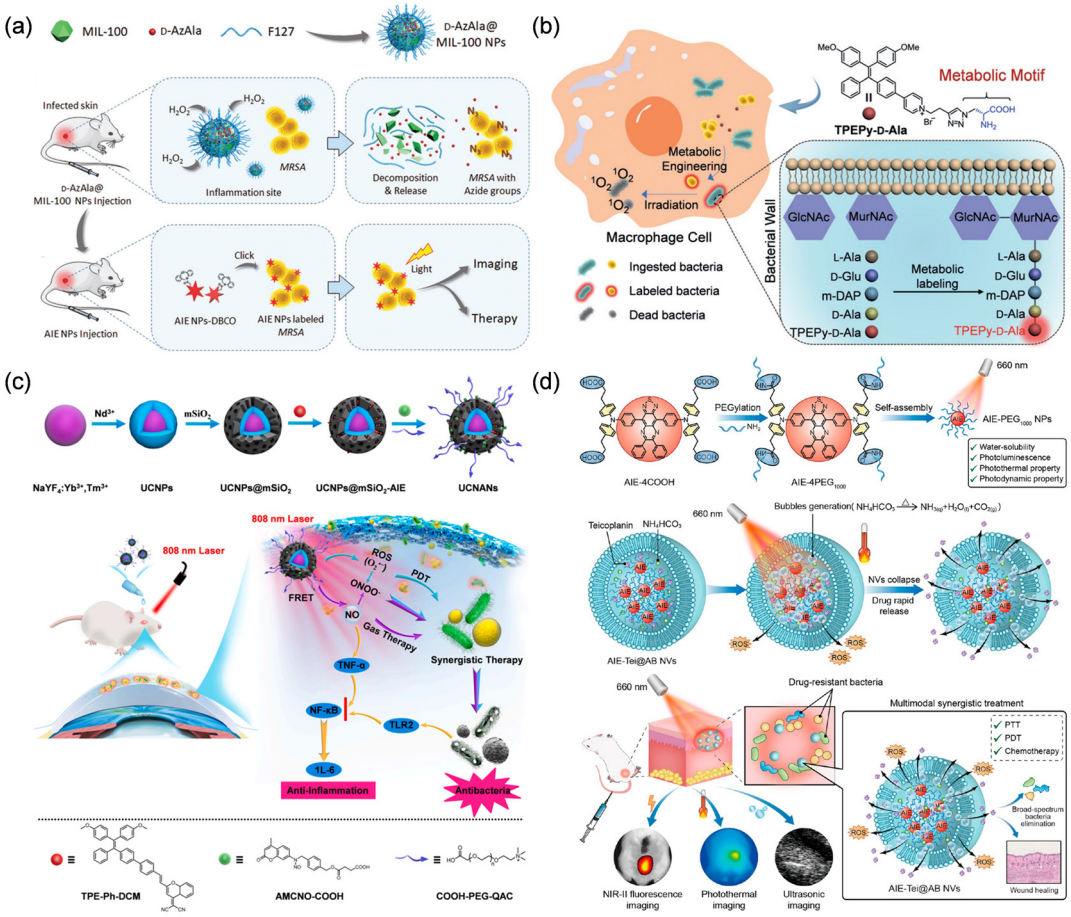

Fig. 10 (a) Schematic illustration of the proposed strategy of bacterial diagnosis and H_2O_2-responsive MOF assisted *in vivo* metabolic labeling of bacteria.[100] Copyright 2018, Wiley-VCH. (b) Schematic illustration of TPEPy-D-Ala as a metabolic probe for visualization and *in situ* ablation of intracellular bacterial pathogens.[101] Copyright 2019, Wiley-VCH. (c) Schematic illustration of the synthetic route to UCNANs and synergistic PDT and NO therapy of refractory keratitis.[104] Copyright 2022, Elsevier. (d) Schematic illustration of the AIE-Tei@AB NVs for trimodal imaging-guided multimodal synergistic therapy of drug-resistant bacterial infections.[105] Copyright 2023, American Chemical Society.

Yb^{3+}) as the light-responsive core and mesoporous silica as the shell to load an AIE-based photosensitizer (TPE-Ph-DCM). Then, the bacterial targeting molecule COOH-PEG-quaternary ammonium compound (COOH-PEG-QAC) and the AMC-based NO donor (AMCNO-COOH) were grafted onto UCNP@$mSiO_2$ *via* an amide reaction. Under the irradiation of NIR light at 808 nm, UCNANs converted NIR photons into ultraviolet and visible photons, which were used to trigger the release of NO by AMCNO and activate TPEPh-DCM to generate ROS (such as $O_2^{\bullet-}$) and NO and can further react with $O_2^{\bullet-}$ to generate highly cytotoxic $ONOO^-$ molecules. For the rat model of refractory *S. aureus* keratitis, after treatment with UCNANs, the slit-lamp score, corneal thickness value, and bacterial counts decreased rapidly, and the corneal clarity and transparency were similar to those of the levofloxacin group, effectively alleviating the symptoms of infection. In addition, bacterial clearance reduced the secretion of endotoxin, and the accompanying release of NO downregulated the expression of toll-like receptor 2 (TRL2) and tumor necrosis factor-α (TNF-α), thereby inhibiting the nuclear factor-κ-gene binding NF-κB pathway, downregulating proinflammatory cytokine (IL6), and significantly relieving corneal inflammation. To improve the spatial resolution and penetration depth of AIEgens in deep tissue diseases, Liao's group devised a novel approach by constructing self-assembled AIE-PEG_{1000} NPs capable of NIR-II fluorescence emission, and photothermal and photodynamic properties (Fig. 10d).[105] The AIE-PEG_{1000} NPs were effectively encapsulated with teicoplanin (Tei) and ammonium bicarbonate (AB) within lipid nanovesicles (NVs), forming a "nanobomb" formulation termed AIE-Tei@AB NVs. This nanobomb exhibited remarkable specificity for targeting MDR bacterial infection sites, facilitated by the NIR-II fluorescence and infrared thermal imaging of the foci by the photoluminescence and photothermal properties of AIE-PEG_{1000} NPs upon 660 nm laser irradiation. Moreover, the encapsulated AB underwent thermal decomposition during the photothermal process, generating a substantial quantity of CO_2/NH_3 bubbles. These bubbles enabled high-performance ultrasound imaging of the infected foci. Thus, the AIE-Tei@AB NVs exhibited effective eradication of MRSA through the trimodal imaging guided

combined photothermal and photodynamic properties, along with the NV disintegration and rapid release of Tei during bubble generation.

Other organic photosensitizers

Several other types of photosensitizers have also achieved good therapeutic effects in the field of antibacterials, including indocyanine green (ICG), BODIPY, and natural photosensitizers.[58,106,107]

Due to the active liver targeting properties and ROS generation ability of ICG, Zhou's group combined ICG with gallium, which showed the ability to disrupt iron-associated metabolism processes in bacteria, to design ICG-Ga NPs. (Fig. 11a).[108] After treatment with ICG-Ga NPs under 808 nm laser irradiation, the original morphology of *E. coli* was distorted, the bacterial cell walls were wrinkled with holes, and the biofilm could be almost completely eliminated. Enhanced Ga^{3+} accumulates on the damaged bacterial membrane, which promotes the endocytosis of Ga^{3+}, and then replaces the iron in the bacterial cells and disrupts bacterial iron metabolism. Furthermore, ICG-Ga NPs could be localized at the liver to treat bacterial infections and subsequently cleared by hepatic and renal metabolism with negligible systemic toxicities. For antimicrobial therapy and inflammation relief in deep infections, Song's group combined UCNPs with partially oxidized SnS_2 (POS) nanosheets (NSs) and ICG to construct the NIR-mediated versatile aPDT nanoplatform POS-UCNPs/ICG (Fig. 11b).[109] UCNPs were able to convert 808 nm NIR light to green light, while 2D POS NSs have high charge separation rates and a long lifetime of charge separation, and therefore have high CO and O_2 production under NIR light irradiation. In the process of aPDT, O_2 could enhance aPDT, and CO could regulate inflammation through the PI3K/NF-KB pathway, making the healing area of the POS-UCNPs/ICG group up to 91.55 ± 1.26% in mouse abscesses. Yang's group synthesized the metabolically labeled photosensitizer IR820-DAA by coupling commercial IR820 with D-propargyl glycine (DAA) in a simple one-step process that could be metabolically incorporated into bacterial walls *via* enzymatic reactions as a synergistic photothermal/photodynamic agent for effective antibacterial therapy and wound healing.[110]

To provide sufficient oxygen and prolong the lifetime of ROS, Bai *et al.* used iodized boron dipyrromethene (BODIPY-I) as a photosensitizer and a perfluoropolyether glycopolymer (PFH) combined with galactose and fucose to form oxygen self-supplying nanotherapeutic PFH/F-I, which could capture *P. aeruginosa* specifically and inhibit bacterial colonization and biofilm formation effectively (Fig. 11c).[111] The large oxygen carrying capacity of PFH/F-I, up to 13 mg mL^{-1}, improves the oxygen concentration around BODIPY, thus increasing ROS pro-

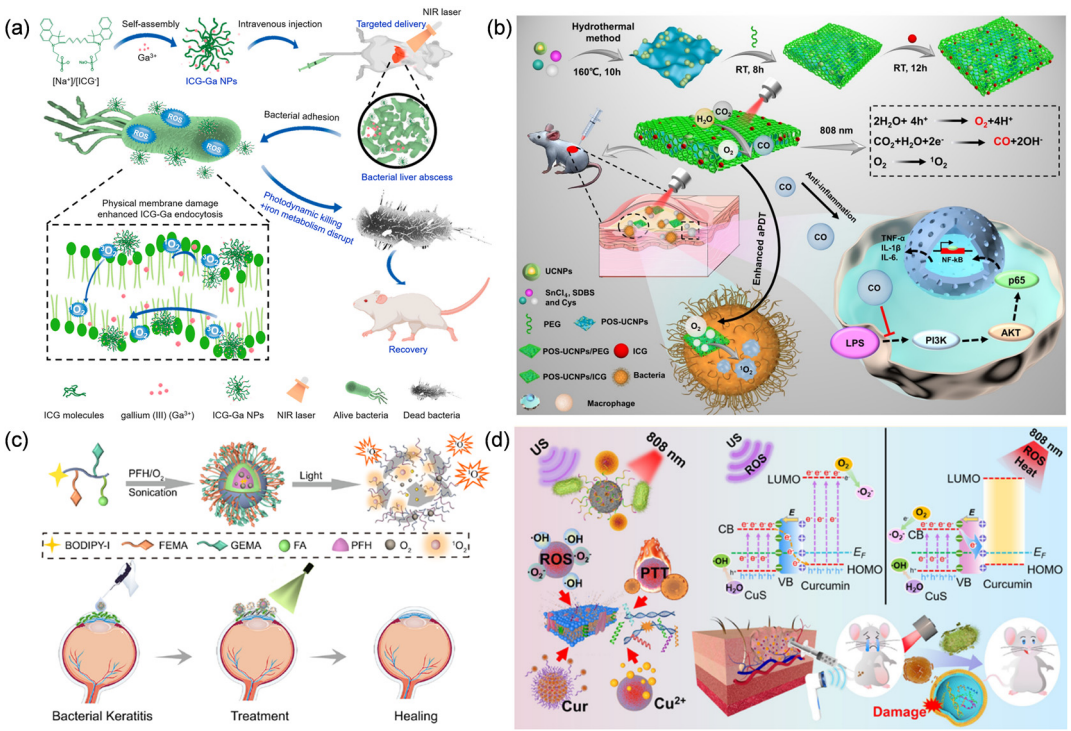

Fig. 11 (a) Schematic illustration of the synthesis of ICG-Ga NPs and treatment of drug-resistant bacterial infected liver abscesses.[108] Copyright 2021, The Authors. (b) Schematic illustration of POS-UCNPs/ICG in preparation, antisepsis and anti-inflammatory mechanisms.[109] Copyright 2022, The Authors. (c) Schematic illustration of self-assembled oxygen self-supplying glycomimetics containing perfluoropolyethers and nanotherapeutic-enhanced antimicrobial PDT in a bacterium-infected keratitis model.[111] Copyright 2021, American Chemical Society. (d) Schematic illustration of the antibacterial mechanism of CuS/Cur.[112] Copyright 2021, American Chemical Society.

Table 1 Summary of the organic photosensitizers for aPDT with application information

Photosensitizer	Therapeutic agent	Light source		Application		Therapeutic modality	Ref.
		Wavelength	Intensity	Organism	Model		
Porphyrins	ZMP	410 ± 15 nm	50 mW cm^{-2}	*S. mutans*	Biofilm on teeth	PDT	40
	Ga-CHP	410 ± 15 nm	50 mW cm^{-2}	*S. aureus*	Full-thickness skin trauma	PDT + IBAT	45
	J-AuPPS	808 nm	1 W cm^{-2}	MRSA	Titanium disk infection	PDT + PTT	46
	TP-Por CON@BNN6	635 nm	1 W cm^{-2}	*S. aureus*	Chronic wounds	PDT + PTT + NO	47
	Co^{II}TBPP(bpy)	660 nm	1 W cm^{-2}	*E. coli*	Skin wounds	PDT	51
	TMPyP	white light	20 mW cm^{-2}	*E. coli*	Subcutaneous abscess	PDT + PTT	52
	TFPP-QA/CP5	660 nm	400 mW cm^{-2}	MRSA, MRSA	Wounds and biofilm catheter	PDT	53
	PDPA-TPP	650 nm	50 mW cm^{-2}	MDR *S. aureus*, MDR *S. aureus*	Wounds and biofilm catheter	PDT	54
Chlorophyll	Pep@Ce6	660 nm	50 mW cm^{-2}	*P. aeruginosa*	Skin knife injury	PDT	59
	Ce6@MnO_2-PEG NPs	661 nm	5 mW cm^{-2}	*S. aureus*	Abscesses	PDT	60
	Ce6@WCS-IONP	660 nm	100 mW cm^{-2}	MRSA	Wounds	PDT	61
	HCM NPs	635 nm	20 mW cm^{-2}	MRSA	Biofilm-infected wounds	PDT + MNZ	63
	CeCyan-$Cu_{5.4}O$	660 nm	200 mW cm^{-2}	*P. acnes*, *S. Gordonii*, *P. gingivalis*, *F. nucleatum*	Keratitis and periodontitis	PDT	64
	Ce6@Arg-ADP	665 nm	115 mW cm^{-2}	MRSA	Subcutaneous abscess	PDT + NO	69
	α-CD-Ce6-NO-DA	660 nm	200 mW cm^{-2}	MRSA	Subcutaneous infection	PDT + NO	70
	Ce6&CO@FADP	665 nm	11 mW cm^{-2}	*E. coli*, *S. aureus*	Knife injury and biofilm catheter	PDT + CO	71
Phenothiazines	NBS-N, NBSe-N	655nm	50 mW cm^{-2}	*S. aureus*	Wounds	PDT	73
	Pyridophenothiaziniums	635 nm	30 J cm^{-2}	*S. aureus*	Wounds	PDT	72
	UCMB-LYZ-HP	980 nm	500 mW cm^{-2}	MRSA	Wounds	PDT + LYZ	74
	MagTBO	664–670nm	180 J cm^{-2}	*S. mutans*	Biofilms	PDT + SPIONs	75
Xanthenes	PαGal_{50}-*b*-$PGRB_{20}$	578 ± 10 nm	60 mW cm^{-2}	MDR *P. aeruginosa*	Biofilm infected keratitis	PDT	77
	PBMA-*b*-P(DMAEMA-*co*-EoS)-UBI	520 ± 10 nm	400 mW cm^{-2}	*P. aeruginosa*, *P. aeruginosa*	Knife injury and burn	PDT	78
	RB@PMB@GA NPs	578 ± 10 nm	60 mW cm^{-2}	*P. aeruginosa*	Biofilm catheters	PDT + PMB	79
	HPT-RP	575 nm	60 mW cm^{-2}	*S. aureus*	Skin defect	PDT + tobramycin	80
Aggregation-induced emission	TBZPyI, CTBZPyI	520 nm	100 mW cm^{-2}	MRSA	Wounds	PDT	93
	TTCPy-1, TTCPy-2, TTCPy-3, TTCPy-4	White light	16 mW cm^{-2}	MDR *E. coli*, MRSA	Wounds	PDT	94
	TPy, TPPy, TTPy, MeOTTPy, TPE-TTP	White light	60 mW cm^{-2}	*S. aureus*	Wounds	PDT	95
	CPVBA, CPVBP, CPVBP2, CPVBP3	400–700 nm	20 mW cm^{-2}	*S. aureus*, *S. epidermidis*, *E. coli*	—	PDT	96
	PTB-APFB	White light	100 mW cm^{-2}	*S. aureus*	Skin wounds	PDT	97
	d-AzAla@MIL-100 (Fe), AIE NPs-DBCO	White light	300 mW cm^{-2}	MRSA	Subcutaneous infection	PDT	100
	TPEPy-D-Ala	White light	60 mW cm^{-2}	MRSA, *E. coli*	Infected RAW 264.7	PDT	101
	TPACN-D-Ala	White light	300 mW cm^{-2}	*S. aureus*	Subcutaneous infection	PDT	102
	TBTCP-PMB engineered phages	White light	80 mW cm^{-2}	*E. coli*, *P. aeruginosa*, *S. typhimurium*, MRSA	Sepsis	PDT + phages	84
	TTPy	White light	20 mW cm^{-2}	*S. aureus*	Endophthalmitis	PDT	103
	UCNANs	808 nm	400 mW cm^{-2}	*S. aureus*	Refractory keratitis	PDT + NO	104

Table 1 *(Contd.)*

Photosensitizer	Therapeutic agent	Light source		Application		Therapeutic modality	Ref.
		Wavelength	Intensity	Organism	Model		
	AIE-Tei@AB NVs	660 nm	800 mW cm^{-2}	MRSA, MDR *E. coli*, MDR *P. aeruginosa*	Subcutaneous abscess	PDT + PTT + teicoplanin	105
Others	ICG-Ga NPs	808 nm	1 W cm^{-2}	ESBL *E. coli*	Liver abscess	PDT + IBAT	108
	POS-UCNPs/ICG	808 nm	1 W cm^{-2}	*S. aureus*	Subcutaneous abscess	PDT + CO	109
	IR820-DAA	808 nm	1 W cm^{-2}	MRSA	Wounds	PDT + PTT	110
	PFH/F-I	532 nm	50 mW cm^{-2}	*P. aeruginosa*	Keratitis	PDT	111
	CuS/Cur	808 nm	500 mW cm^{-2}	*S. aureus*	Wounds	PDT + PTT + SDT	112

duction and effectively alleviating the anoxic microenvironment at the site of inflammation. PFH/F-I downregulated the expression of HIF-1α in rats infected with *P. aeruginosa* keratitis, and reduced the levels of inflammatory cytokines in the cornea (such as TNF-α, IL-6 and MMP-9) to the level of healthy corneal tissue. After treatment with PFH/F-I, the corneal structure remained normal, and bacterial-induced tissue collagen breakdown and structural alignment alterations were mitigated.

As a natural photosensitizer, curcumin (Cur) is a kind of compound with a diketone structure extracted from the rhizomes of the ginger family and the araceae family that has anti-inflammatory, antioxidant and anti-tumor activities. Due to its organic semiconductor properties, Cur is sensitive to light and produces ROS. CuS, as a p-type semiconductor, has a narrow band gap and exhibits good photothermal or photodynamic effects under light irradiation at different wavelengths. At the same time, Cu^{2+}, as one of the essential trace elements, plays a variety of significant physiological and pharmacological functions in the human body (such as combining with various enzymes and proteins in the body to participate in metabolic processes). Wu's group used a photoacoustic interfacial engineering strategy to combine Cur and CuS to form CuS/Cur hybrid materials with tight contacts through *in situ* nucleation and growth on the surface of petaloid CuS (Fig. 11d).[112] The CuS/Cur hybrids not only exerted the pharmaceutical properties of Cur, but also exhibited photo-sono responsive ability, which enables the hybrids to produce a good killing effect on *S. aureus* and *E. coli* through photothermal, photodynamic and sonodynamic therapy (SDT).

In vivo biosafety of photosensitizers

The evaluation of *in vivo* biosafety of organic photosensitizers is crucial for advancing their clinical translation. The nonspecific accumulation of organic photosensitizers in the liver and spleen, coupled with their slow and inefficient clearance, necessitates the examination of liver function tests including alanine aminotransferase (ALT) and aspartate aminotransferase (AST). To investigate the *in vivo* biocompatibility of Ga-CHP, Zhang's group administered Ga-CHP intravenously in healthy mice.[45] The biochemical assay results showed that hepatic function indices such as albumin (ALB) and ALT, myocardial enzyme-related indices such as AST and lactate dehydrogenase (LDH), and renal function indices such as serum creatinine (Cr) and blood urea nitrogen (BUN) did not induce significant adverse reactions after 14 days. Accompanying this, hematoxylin and Eosin (H&E) staining images of different organs did not show pathological features and the body weight of mice increased slightly. Similarly, Liu *et al.* estimated a series of physiological and biochemical indicators associated with kidney and liver function at the end of CTBZPyI treatment in infected mice at day 11, which were all within the normal ranges.[93] There were also no obvious morphological changes or inflammatory lesions in the major organs of the mice observed in H&E staining.

The development of organic photosensitizers with renal clearance or biodegradation capability presents a promising approach to enhance the elimination of these agents from the body. To address this challenge, Yang's group engineered a nanophotosensitizer featuring three hydrophilic triethylene glycol arms and two cationic pyridinium groups in an aqueous medium.[113] Notably, the nanophotosensitizer exhibited an ultra-small size, with an average diameter of 5.6 nm, facilitating its clearance *via* urinary excretion with reduced nonspecific accumulation. To further enhance the post-operative safety of aPDT, Liu's group designed a series of self-degradable D–A photosensitizers.[114] With self-produced $^1O_2$, these photosensitizers were capable of oxidizing anthracene bridges, resulting in the formation of endoperoxide- and anthrone-derived fragments and the disruption of π-conjugation, thus enabling rapid clearance.

Conclusions

This review summarizes the recent advances in organic photosensitizers for aPDT, including porphyrins, chlorophyll, phenothiazines, xanthenes and aggregation-induced emission photosensitizers. Diverse strategies have been designed to amplify the therapeutic effects of photosensitizers based on the hypoxic, acidic, and H_2O_2-overexpressed microenvironment at the site of infection, as well as the unique structure of bacteria, resulting in more effective bacterial elimination. Moreover, this review discussed the efficacy of combining aPDT with other therapies, including antimicrobial peptide

therapy, PTT or gas therapy. The corresponding photosensitizers, therapeutic agents, light sources, applications and therapeutic modalities are listed in Table 1.

Although numerous photosensitizers for aPDT have been approved in clinical trials, there remain inherent issues that need to be addressed. First, many photosensitizers have excitation wavelengths confined to the visible region, limiting their efficacy against deep-seated infections such as pneumonia and enteritis. As such, the development of near-infrared photosensitizers or a switch to SDT is necessary.[115–119] Second, although aPDT alone is effective against Gram-positive bacteria, it is often inadequate against Gram-negative bacteria due to their unique outer membrane structure.[120] Consequently, the development of photosensitizers with destructive effects on the outer membrane is imperative. Furthermore, most reported photosensitizers rely solely on positive charge targeting, which is inadequate for *in vivo* application, even though mammalian cell membranes are less negatively charged than bacteria cell membranes.[121,122] Therefore, there is an urgent need for the continuous development of specific targets to improve bacterial targeting.[123] Finally, systemic toxicity risk is a significant concern when applying photosensitizers to treat *in vivo* infections.[113,114] Despite these challenges, aPDT has shown promising preliminary results, and with further exploration and optimization, it is expected to play a more significant role in the clinical treatment of bacterial infections.

Conflicts of interest

There are no conflicts to declare.

Acknowledgements

X. Z. thanks the National Key R & D Program of China (No. 2022YFB3804600), the National Natural Science Foundation of China (No. 51903120, 52173130), the State Key Laboratory of Analytical Chemistry for Life Science (No. SKLACL2212) and the Fundamental Research Funds for the Central Universities (No. 020514380274) for the financial support.

References

1 Y. Ma, Z. Guo, B. Xia, Y. Zhang, X. Liu, Y. Yu, N. Tang, X. Tong, M. Wang, X. Ye, J. Feng, Y. Chen and J. Wang, *Nat. Biotechnol.*, 2022, **40**, 921–931.
2 K. D. Roberts, Y. Zhu, M. A. K. Azad, M. L. Han, J. Wang, L. Wang, H. H. Yu, A. S. Horne, J. A. Pinson, D. Rudd, N. H. Voelcker, N. A. Patil, J. Zhao, X. Jiang, J. Lu, K. Chen, O. Lomovskaya, S. J. Hecker, P. E. Thompson, R. L. Nation, M. N. Dudley, D. C. Griffith, T. Velkov and J. Li, *Nat. Commun.*, 2022, **13**, 1625.
3 B. H. Gan, J. Gaynord, S. M. Rowe, T. Deingruber and D. R. Spring, *Chem. Soc. Rev.*, 2021, **50**, 7820–7880.
4 Y. Qian, S. Deng, Z. Cong, H. Zhang, Z. Lu, N. Shao, S. A. Bhatti, C. Zhou, J. Cheng, S. H. Gellman and R. Liu, *J. Am. Chem. Soc.*, 2022, **144**, 1690–1699.
5 Z. Geng, Z. Cao and J. Liu, *Exploration*, 2023, **3**, 20210117.
6 X. Li, H. Bai, Y. Yang, J. Yoon, S. Wang and X. Zhang, *Adv. Mater.*, 2019, **31**, 1805092.
7 H. Hu, D. Zhong, W. Li, X. Lin, J. He, Y. Sun, Y. Wu, M. Shi, X. Chen, F. Xu and M. Zhou, *Nano Today*, 2022, **42**, 101368.
8 K. Sauer, P. Stoodley, D. M. Goeres, L. Hall-Stoodley, M. Burmolle, P. S. Stewart and T. Bjarnsholt, *Nat. Rev. Microbiol.*, 2022, **20**, 608–620.
9 A. Vishwakarma, F. Dang, A. Ferrell, H. A. Barton and A. Joy, *J. Am. Chem. Soc.*, 2021, **143**, 9440–9449.
10 S. Mu, Y. Zhu, Y. Wang, S. Qu, Y. Huang, L. Zheng, S. Duan, B. Yu, M. Qin and F. J. Xu, *Adv. Mater.*, 2022, **34**, 2204065.
11 T. A. Wencewicz, *J. Mol. Biol.*, 2019, **431**, 3370–3399.
12 H. C. S. Carneiro, R. W. Bastos, N. Q. Ribeiro, L. Gouveia-Eufrasio, M. C. Costa, T. F. F. Magalhaes, L. V. N. Oliveira, T. A. Paixao, L. S. Joffe, M. L. Rodrigues, G. R. S. Araujo, S. Frases, J. C. Ruiz, P. Marinho, J. S. Abrahao, M. A. Resende-Stoianoff, D. Carter and D. A. Santos, *Sci. Total Environ.*, 2020, **740**, 140135.
13 A. J. Schaenzer and G. D. Wright, *Trends Mol. Med.*, 2020, **26**, 768–782.
14 J. Hu, Q. Lei and X. Zhang, *Prog. Mater. Sci.*, 2020, **114**, 100685.
15 L. Huang, S. Zhao, J. Wu, L. Yu, N. Singh, K. Yang, M. Lan, P. Wang and J. S. Kim, *Coord. Chem. Rev.*, 2021, **438**, 213888.
16 Y. Liu, X. Meng and W. Bu, *Coord. Chem. Rev.*, 2019, **379**, 82–98.
17 M. Wu, R. Qu, H. Li, L. Chen, X. Zhang, Y. Yuan, W. Chen, X. Jiang and X. Zhen, *Nano Today*, 2023, **48**, 101691.
18 X. Zhen, C. Xie, Y. Jiang, X. Ai, B. Xing and K. Pu, *Nano Lett.*, 2018, **18**, 1498–1505.
19 X. Zhen, C. Xie and K. Pu, *Angew. Chem., Int. Ed.*, 2018, **57**, 3938–3942.
20 X. Zhen, J. Zhang, J. Huang, C. Xie, Q. Miao and K. Pu, *Angew. Chem., Int. Ed.*, 2018, **57**, 7804–7808.
21 N. Yang, C. Cao, X. Lv, T. Zhang, J. Shao, X. Song, W. Wang, P. Chen, W. Huang and X. Dong, *BMEMat*, 2023, **1**, e12005.
22 H. Wang, Z. He, X.-A. Liu, Y. Huang, J. Hou, W. Zhang and D. Ding, *Small Struct.*, 2022, **3**, 2200036.
23 J. Xie, Y. Wang, W. Choi, P. Jangili, Y. Ge, Y. Xu, J. Kang, L. Liu, B. Zhang, Z. Xie, J. He, N. Xie, G. Nie, H. Zhang and J. S. Kim, *Chem. Soc. Rev.*, 2021, **50**, 9152–9201.
24 M. Piksa, C. Lian, I. C. Samuel, K. J. Pawlik, I. D. W. Samuel and K. Matczyszyn, *Chem. Soc. Rev.*, 2023, **52**, 1697–1722.
25 G. Kassab, J. S. D. Tovar, L. M. P. Souza, R. K. M. Costa, R. S. Silva, A. S. Pimentel, C. Kurachi and V. S. Bagnato, *Proc. Natl. Acad. Sci. U. S. A.*, 2022, **119**, e2123564119.

26 X. Li, B. Zheng, X. Peng, S. Li, J. Ying, Y. Zhao, J. Huang and J. Yoon, *Coord. Chem. Rev.*, 2019, **379**, 147–160.
27 G. Feng, G. Q. Zhang and D. Ding, *Chem. Soc. Rev.*, 2020, **49**, 8179–8234.
28 X. Hu, H. Zhang, Y. Wang, B. Shiu, J. Lin, S. Zhang, C. Lou and T. Li, *Chem. Eng. J.*, 2022, **450**, 138129.
29 J. Zhang, Q. Jia, Z. Yue, J. Huo, J. Chai, L. Yu, R. Nie, H. Shao, Y. Zhao, P. Li and W. Huang, *Adv. Mater.*, 2022, **34**, 2200334.
30 Q. Jia, Q. Song, P. Li and W. Huang, *Adv. Healthcare Mater.*, 2019, **8**, 1900608.
31 J. Zhang, C. Jiang, J. P. F. Longo, R. B. Azevedo, H. Zhang and L. A. Muehlmann, *Acta Pharm. Sin. B*, 2018, **8**, 137–146.
32 E. Pang, S. Zhao, B. Wang, G. Niu, X. Song and M. Lan, *Coord. Chem. Rev.*, 2022, **472**, 214780.
33 M. Tavakkoli Yaraki, B. Liu and Y. N. Tan, *Nano-Micro Lett.*, 2022, **14**, 123.
34 E. Lei, H. Tao, S. Jiao, A. Yang, Y. Zhou, M. Wang, K. Wen, Y. Wang, Z. Chen, X. Chen, J. Song, C. Zhou, W. Huang, L. Xu, D. Guan, C. Tan, H. Liu, Q. Cai, K. Zhou, J. Modica, S. Y. Huang, W. Huang and X. Feng, *J. Am. Chem. Soc.*, 2022, **144**, 10622–10639.
35 Y. Qiao, Y. Xu, X. Liu, Y. Zheng, B. Li, Y. Han, Z. Li, K. W. K. Yeung, Y. Liang, S. Zhu, Z. Cui and S. Wu, *Nat. Commun.*, 2022, **13**, 2461.
36 Y. Gao, J. Wang, M. Chai, X. Li, Y. Deng, Q. Jin and J. Ji, *ACS Nano*, 2020, **14**, 5686–5699.
37 B. Ran, Z. Wang, W. Cai, L. Ran, W. Xia, W. Liu and X. Peng, *J. Am. Chem. Soc.*, 2021, **143**, 17891–17909.
38 Q. Jia, Q. Song, P. Li and W. Huang, *Adv. Healthcare Mater.*, 2019, **8**, 1900608.
39 V. N. Nguyen, Z. Zhao, B. Z. Tang and J. Yoon, *Chem. Soc. Rev.*, 2022, **51**, 3324–3340.
40 H. Zhang, Y. Zhu, Y. Li, X. Qi, J. Yang, H. Qi, Q. Li, Y. Ma, Y. Zhang, X. Zhang and L. Zhang, *Adv. Funct. Mater.*, 2021, **31**, 2104799.
41 H. Yang, R. Liu, Y. Xu, L. Qian and Z. Dai, *Nano-Micro Lett.*, 2021, **13**, 35.
42 X. Zhen, P. Cheng and K. Pu, *Small*, 2019, **15**, 1804105.
43 S. Chen, Z. Chu, L. Cao, L. Xu, Q. Jin, N. Liu, B. Chen, M. Fang, W. Wang, H. Qian and M. Shao, *Nano Res.*, 2022, **15**, 9298–9308.
44 W. Wang, P. Pei, Z. Chu, B. Chen, H. Qian, Z. Zha, W. Zhou, T. Liu, M. Shao and H. Wang, *Chem. Eng. J.*, 2020, **397**, 125488.
45 H. Zhang, Q. Li, X. Qi, Y. Li, H. Ma, M. Grinholc, J. Nakonieczna, B. Yu, X. Wang and L. Zhang, *Chem. Eng. J.*, 2023, **451**, 138261.
46 C. Chen, G. Chu, W. He, Y. Liu, K. Dai, J. Valdez, A. Moores, P. Huang, Z. Wang, J. Jin, M. Guan, W. Jiang, Y. Mai, D. Ma, Y. Wang and Y. Zhou, *Adv. Mater.*, 2023, **35**, 2207950.
47 B. Sun, Z. Ye, M. Zhang, Q. Song, X. Chu, S. Gao, Q. Zhang, C. Jiang, N. Zhou, C. Yao and J. Shen, *ACS Appl. Mater. Interfaces*, 2021, **13**, 42396–42410.
48 M. Ye, Y. Zhao, Y. Wang, M. Zhao, N. Yodsanit, R. Xie, D. Andes and S. Gong, *Adv. Mater.*, 2021, **33**, 2006772.
49 Q. Zeng, X. Qi, G. Shi, M. Zhang and H. Haick, *ACS Nano*, 2022, **16**, 1708–1733.
50 S. Jia, S. Ji, J. Zhao, Y. Lv, J. Wang, D. Sun and D. Ding, *Small Methods*, 2023, **7**, 2201409.
51 Y. Hu, W. Wang, S. Huang, J. Li, Y. Zhang, Y. Gao, Y. Cheng, Z. Wu and X. Zhang, *Chem. Eng. J.*, 2022, **431**, 133704.
52 H. Hu, H. Wang, Y. Yang, J. F. Xu and X. Zhang, *Angew. Chem., Int. Ed.*, 2022, **61**, e202200799.
53 L. Xia, J. Tian, T. Yue, H. Cao, J. Chu, H. Cai and W. Zhang, *Adv. Healthcare Mater.*, 2022, **11**, 2102015.
54 F. Yu, C. Chen, G. Yang, Z. Ren, H. Cao, L. Zhang and W. Zhang, *Sci. China: Chem.*, 2021, **64**, 459–466.
55 N. Suvorov, V. Pogorilyy, E. Diachkova, Y. Vasil'ev, A. Mironov and M. Grin, *Int. J. Mol. Sci.*, 2021, **22**, 6392.
56 C. Pucci, C. Martinelli, A. Degl'Innocenti, A. Desii, D. De Pasquale and G. Ciofani, *Macromol. Biosci.*, 2021, **21**, 2100181.
57 Y. Zhang, S. Chen, Q. Xia, H. Zhang, Z. Wang, R. Yan, X. Zhang, J. Dai, X. Wu, W. Fang and Y. Jin, *Process Biochem.*, 2022, **122**, 363–373.
58 T. C. Pham, V. N. Nguyen, Y. Choi, S. Lee and J. Yoon, *Chem. Rev.*, 2021, **121**, 13454–13619.
59 Q. Gao, D. Huang, Y. Deng, W. Yu, Q. Jin, J. Ji and G. Fu, *Chem. Eng. J.*, 2021, **417**, 129334.
60 C. Wang, Y. Xiao, W. Zhu, J. Chu, J. Xu, H. Zhao, F. Shen, R. Peng and Z. Liu, *Small*, 2020, **16**, 2000589.
61 Y. Jin, B. Zhao, W. Guo, Y. Li, J. Min and W. Miao, *J. Controlled Release*, 2022, **348**, 911–923.
62 Y. Wan, L. H. Fu, C. Li, J. Lin and P. Huang, *Adv. Mater.*, 2021, **33**, 2103978.
63 W. Xiu, L. Wan, K. Yang, X. Li, L. Yuwen, H. Dong, Y. Mou, D. Yang and L. Wang, *Nat. Commun.*, 2022, **13**, 3875.
64 B. Wang, L. Zhou, Y. Guo, H. Guo, Y. Zhong, X. Huang, Y. Ge, Q. Wang, X. Chu, Y. Jin, K. Lan, M. Yang and J. Qu, *Bioact. Mater.*, 2022, **12**, 314–326.
65 X. Bao, S. Zheng, L. Zhang, A. Shen, G. Zhang, S. Liu and J. Hu, *Angew. Chem., Int. Ed.*, 2022, **61**, e202207250.
66 Z. Chen, S. Zheng, Z. Shen, J. Cheng, S. Xiao, G. Zhang, S. Liu and J. Hu, *Angew. Chem., Int. Ed.*, 2022, **61**, e202204526.
67 L. Gao, J. Cheng, Z. Shen, G. Zhang, S. Liu and J. Hu, *Angew. Chem., Int. Ed.*, 2022, **61**, e202112782.
68 H. Wu, D. Zhong, Z. Zhang, Y. Wu, Y. Li, H. Mao, K. Luo, D. Kong, Q. Gong and Z. Gu, *ACS Nano*, 2021, **15**, 4845–4860.
69 J. Zhu, J. Tian, C. Yang, J. Chen, L. Wu, M. Fan and X. Cai, *Small*, 2021, **17**, 2101495.
70 D. Hu, Y. Deng, F. Jia, Q. Jin and J. Ji, *ACS Nano*, 2020, **14**, 347–359.
71 W. Ma, X. Chen, L. Fu, J. Zhu, M. Fan, J. Chen, C. Yang, G. Yang, L. Wu, G. Mao, X. Yang, X. Mou, Z. Gu and X. Cai, *ACS Appl. Mater. Interfaces*, 2020, **12**, 22479–22491.

72 Q. Xiao, B. Mai, Y. Nie, C. Yuan, M. Xiang, Z. Shi, J. Wu, W. Leung, C. Xu, S. Q. Yao, P. Wang and L. Gao, *ACS Appl. Mater. Interfaces*, 2021, **13**, 11588–11596.
73 X. Wu, M. Yang, J. S. Kim, R. Wang, G. Kim, J. Ha, H. Kim, Y. Cho, K. T. Nam and J. Yoon, *Angew. Chem., Int. Ed.*, 2022, **61**, e202200808.
74 Z. Li, S. Lu, W. Liu, T. Dai, J. Ke, X. Li, R. Li, Y. Zhang, Z. Chen and X. Chen, *Angew. Chem., Int. Ed.*, 2021, **60**, 19201–19206.
75 A. A. Balhaddad, Y. Xia, Y. Lan, L. Mokeem, M. S. Ibrahim, M. D. Weir, H. H. K. Xu and M. A. S. Melo, *ACS Nano*, 2021, **15**, 19888–19904.
76 K. Huang, J. Wang, Q. Zhang, K. Yuan, Y. Yang, F. Li, X. Sun, H. Chang, Y. Liang, J. Zhao, T. Tang and S. Yang, *Adv. Funct. Mater.*, 2022, **32**, 2204906.
77 Y. Zhu, S. Wu, Y. Sun, X. Zou, L. Zheng, S. Duan, J. Wang, B. Yu, R. Sui and F. J. Xu, *Adv. Funct. Mater.*, 2021, **32**, 2111066.
78 F. Xiao, B. Cao, C. Wang, X. Guo, M. Li, D. Xing and X. Hu, *ACS Nano*, 2020, **13**, 1511–1525.
79 S. Wu, C. Xu, Y. Zhu, L. Zheng, L. Zhang, Y. Hu, B. Yu, Y. Wang and F. J. Xu, *Adv. Funct. Mater.*, 2021, **31**, 2103591.
80 M. Shao, Y. Fan, K. Zhang, Y. Hu and F.-J. Xu, *Nano Today*, 2021, **39**, 101224.
81 H. Bai, W. He, J. H. C. Chau, Z. Zheng, R. T. K. Kwok, J. W. Y. Lam and B. Z. Tang, *Biomaterials*, 2021, **268**, 120598.
82 X. Chen, H. Han, Z. Tang, Q. Jin and J. Ji, *Adv. Healthcare Mater.*, 2021, **10**, 2100736.
83 X. He, Y. Yang, Y. Guo, S. Lu, Y. Du, J. J. Li, X. Zhang, N. L. C. Leung, Z. Zhao, G. Niu, S. Yang, Z. Weng, R. T. K. Kwok, J. W. Y. Lam, G. Xie and B. Z. Tang, *J. Am. Chem. Soc.*, 2020, **142**, 3959–3969.
84 M. Y. Wu, L. Chen, Q. Chen, R. Hu, X. Xu, Y. Wang, J. Li, S. Feng, C. Dong, X. L. Zhang, Z. Li, L. Wang, S. Chen and M. Gu, *Adv. Mater.*, 2023, **35**, 2208578.
85 X. Zhen, R. Qu, W. Chen, W. Wu and X. Jiang, *Biomater. Sci.*, 2021, **9**, 285–300.
86 Y. Wu, J. Li, Z. Shen, D. Wang, R. Dong, J. Zhang, Y. Pan, Y. Li, D. Wang and B. Z. Tang, *Angew. Chem., Int. Ed.*, 2022, **61**, e202212386.
87 J. Qi, H. Ou, Q. Liu and D. Ding, *Aggregate*, 2021, **2**, 95–113.
88 J. Li, H. Gao, R. Liu, C. Chen, S. Zeng, Q. Liu and D. Ding, *Sci. China: Chem.*, 2020, **63**, 1428–1434.
89 H. Gao, X. Qi, J. Zhang, N. Wang, J. Xin, D. Jiao, K. Liu, J. Qi, Y. Guan and D. Ding, *Small Methods*, 2023, **7**, 2201582.
90 R. Qu, X. Zhen and X. Jiang, *CCS Chem.*, 2022, **4**, 401–419.
91 X. Wang, X. Zhen and X. Jiang, *Acta Polym. Sin.*, 2021, **52**, 687–707.
92 J. Li, Z. Zhuang, Z. Zhao and B. Z. Tang, *View*, 2021, **3**, 20200121.
93 S. Liu, B. Wang, Y. Yu, Y. Liu, Z. Zhuang, Z. Zhao, G. Feng, A. Qin and B. Z. Tang, *ACS Nano*, 2022, **16**, 9130–9141.
94 P. Xiao, Z. Shen, D. Wang, Y. Pan, Y. Li, J. Gong, L. Wang, D. Wang and B. Z. Tang, *Adv. Sci.*, 2022, **9**, 2104079.
95 M. Kang, C. Zhou, S. Wu, B. Yu, Z. Zhang, N. Song, M. M. S. Lee, W. Xu, F. J. Xu, D. Wang, L. Wang and B. Z. Tang, *J. Am. Chem. Soc.*, 2019, **141**, 16781–16789.
96 H. Shi, X. Pan, Y. Wang, H. Wang, W. Liu, L. Wang and Z. Chen, *ACS Appl. Mater. Interfaces*, 2022, **14**, 17055–17064.
97 T. Zhou, R. Hu, L. Wang, Y. Qiu, G. Zhang, Q. Deng, H. Zhang, P. Yin, B. Situ, C. Zhan, A. Qin and B. Z. Tang, *Angew. Chem., Int. Ed.*, 2020, **59**, 9952–9956.
98 X. Nie, F. Gao, W. You, G. Chen, Q. Shao, L. Wang, W. Huang, L. Xia, Z. Zhang, C. Hong and Y. You, *Chem. Eng. J.*, 2022, **450**, 138373.
99 H. Jia, Y. Zhu, Y. Liu, Y. Guo, S. M. Sayed, X. Zhu, X. Cheng and F. G. Wu, *Exploration*, 2022, **2**, 20220010.
100 D. Mao, F. Hu, Kenry, S. Ji, W. Wu, D. Ding, D. Kong and B. Liu, *Adv. Mater.*, 2018, **30**, 1706831.
101 F. Hu, G. Qi, Kenry, D. Mao, S. Zhou, M. Wu, W. Wu and B. Liu, *Angew. Chem., Int. Ed.*, 2020, **59**, 9288–9292.
102 D. Mao, F. Hu, Kenry, G. Qi, S. Ji, W. Wu, D. Kong and B. Liu, *Mater. Horiz.*, 2020, **7**, 1138–1143.
103 T. Li, Y. Wu, W. Cai, D. Wang, C. Ren, T. Shen, D. Yu, S. Qiang, C. Hu, Z. Zhao, J. Yu, C. Peng and B. Z. Tang, *Adv. Sci.*, 2022, **9**, 2202485.
104 H. Zhang, W. Jiang, Y. Peng, J. Yang, X. Chu, Z. Long, R. Li, Q. Liang, H. Suo, S. Wang, M. Yang, J. Qi, D. Ding, Y. W. Yang and B. Wang, *Biomaterials*, 2022, **286**, 121577.
105 B. Li, W. Wang, L. Zhao, D. Yan, X. Li, Q. Gao, J. Zheng, S. Zhou, S. Lai, Y. Feng, J. Zhang, H. Jiang, C. Long, W. Gan, X. Chen, D. Wang, B. Z. Tang and Y. Liao, *ACS Nano*, 2023, **17**, 4601–4618.
106 Q. Yang, A. K. Farha, G. Kim, K. Gul, R. Gan and H. Corke, *Trends Food Sci. Technol.*, 2020, **97**, 341–354.
107 J. Wu, J. Sha, C. Zhang, W. Liu, X. Zheng and P. Wang, *View*, 2020, **1**, 20200090.
108 T. Xie, Y. Qi, Y. Li, F. Zhang, W. Li, D. Zhong, Z. Tang and M. Zhou, *Bioact. Mater.*, 2021, **6**, 3812–3823.
109 B. Zhou, X. Sun, B. Dong, S. Yu, L. Cheng, S. Hu, W. Liu, L. Xu, X. Bai, L. Wang and H. Song, *Theranostics*, 2022, **12**, 2580–2597.
110 N. Li, G. Wu, L. Tang, W. Zhou, S. Yang, Q. Pan, M. Wang, P. Wu, H. Xiao, Y. He, X. Tan and Q. Yang, *ACS Appl. Mater. Interfaces*, 2022, **14**, 46362–46373.
111 Y. Bai, Y. Hu, Y. Gao, X. Wei, J. Li, Y. Zhang, Z. Wu and X. Zhang, *ACS Appl. Mater. Interfaces*, 2021, **13**, 33790–33801.
112 H. Liu, J. Li, X. Liu, Z. Li, Y. Zhang, Y. Liang, Y. Zheng, S. Zhu, Z. Cui and S. Wu, *ACS Nano*, 2021, **15**, 18505–18519.
113 D. Zhang, K. X. Teng, L. Zhao, L. Y. Niu and Q. Z. Yang, *Adv. Mater.*, 2023, **35**, 2209789.
114 J. Gao, H. Yang, Y. Lu, Q. Shi, S. Xu, W. Wu, F. Hu and B. Liu, *Chem. Mater.*, 2023, **35**, 1229–1237.
115 S. Roy, I. Hasan and B. Guo, *Coord. Chem. Rev.*, 2023, **482**, 215075.

116 X. Wang, M. Wu, H. Li, J. Jiang, S. Zhou, W. Chen, C. Xie, X. Zhen and X. Jiang, *Adv. Sci.*, 2022, **9**, 2104125.
117 H. Zhang, X. Pan, Q. Wu, J. Guo, C. Wang and H. Liu, *Exploration*, 2021, **1**, 20210010.
118 L. K. B. Tam, J. C. H. Chu, L. He, C. Yang, K. C. Han, P. C. K. Cheung, D. K. P. Ng and P. C. Lo, *J. Am. Chem. Soc.*, 2023, **145**, 7361–7375.
119 S. Jia, Z. Gao, Z. Wu, H. Gao, H. Wang, H. Ou and D. Ding, *CCS Chem.*, 2022, **4**, 501–514.
120 S. Gnanasekar, G. Kasi, X. He, K. Zhang, L. Xu and E. T. Kang, *Bioact. Mater.*, 2023, **21**, 157–174.
121 J. Wang, F. Xia, Y. Wang, H. Shi, L. Wang, Y. Zhao, J. Song, M. Wu and S. Feng, *ACS Appl. Mater. Interfaces*, 2023, **15**, 17433–17443.
122 H. Chen, S. Li, M. Wu, Kenry, Z. Huang, C. S. Lee and B. Liu, *Angew. Chem., Int. Ed.*, 2020, **59**, 632–636.
123 S. Zeng, Z. Wang, C. Chen, X. Liu, Y. Wang, Q. Chen, J. Wang, H. Li, X. Peng and J. Yoon, *Adv. Healthcare Mater.*, 2022, **11**, 2200837.